This is a repository copy of *An experimental and numerical investigation of the use of liquid flow in serpentine microchannels for microelectronics cooling*.

White Rose Research Online URL for this paper:
http://eprints.whiterose.ac.uk/111922/

Version: Accepted Version

Article:

An experimental and numerical investigation of the use of liquid flow in serpentine microchannels for microelectronics cooling

Ahmed F. Al-Neama [a, b, *], Nikil Kapur [a], Jonathan Summers [a], Harvey M. Thompson [a]

[a] Institute of Thermofluids, School of Mechanical Engineering, University of Leeds, LS2 9JT, United Kingdom.

[b] Department of Mechanical Engineering, Faculty of Engineering, University of Mosul, Iraq.

*Corresponding author. Email: ahmedfalneama@gmail.com

Abstract:

This paper presents a combined experimental and numerical investigation of single-phase water flow and heat transfer in serpentine rectangular microchannels embedded in a heated copper block. The performance of four different microchannel heat sink (MCHS) configurations are investigated experimentally, the first having an array of straight rectangular microchannels (SRMs), while the other have single (SPSMs), double (DPSMs) and triple path multi-serpentine rectangular microchannels (TPSMs). Three-dimensional conjugate heat transfer models are developed for both laminar and turbulent single-phase water flows in each of these MCHSs and the governing flow and energy equations solved numerically using finite elements. The numerical predictions of pressure drop (ΔP) and average Nusselt number (Nu_{avg}) are in good agreement with experimental data, and indicated that the single path serpentine microchannel (SPSM) leads to a 35% enhancement of the Nu_{avg} at a volumetric flow rate of 0.5 l/min and a 19% reduction in total thermal resistance (R_{th}) compared to the conventional SRM heat sink. However, this enhancement is at the expense of a large (up to ten-fold) increase in ΔP compared to the SRM heat sink, so that a suitable compromise must be struck between heat transfer and pressure drop in practical MCHS designs.

Keywords: Experiments, Conjugate Heat Transfer, CFD, Serpentine MCHS.

1. Introduction

The increasing density of transistors in electronic components and products is leading to an inexorable rise in the heat dissipation that must be achieved in order to preserve reliability and performance. The International Technology Roadmap for Semiconductors (ITRS) in 2010, for example, predicted a continuous increase in transistor density to reach 10 billion transistors/cm^2, by 2018 [1]. For this reason, improving the thermal management of electronic devices is a crucial goal for future generation of electronic systems. Single-phase microchannel heat sinks (MCHSs) with water as a coolant are an increasingly common means of cooling electronic devices because of their ability to provide very high convective heat transfer fluxes. Single-phase MCHSs rely on sensible heating achieve the cooling, where high heat transfer coefficients (h) can be achieved simply by using small microchannel dimension [2]. Flow boiling (Two-phase flow) MCHSs, on the other hand, have also received much attention from researchers due to their ability to dissipate high heat fluxes with lower pumping powers compared with single-phase liquid MCHSs, by utilising the coolant's latent heat [3]. However, pressure fluctuations and flow reversal associated with flow boiling instabilities can reduce the heat transfer characteristics in MCHS [4].

The use of single-phase MCHS was proposed by Tuckerman and Pease [5] in 1981, who used a water-cooled heat sink, fabricated with an array of SRMs etched in a 1cm^2 silicon wafer. Their pioneering work stimulated many researchers to investigate the fluid flow and thermal performance of the MCHS using different substrate materials with various cooling liquids, see e.g. the recent review of Salman et al. [6] Another major milestone was the experimental study of Phillips [7] on rectangular MCHS test section with an Indium Phosphide heat sink substrate and water as a coolant. Subsequently, a computer model was developed to predict the thermal and flow characteristics of this MCHS, under fully developed

and developing flow conditions for both laminar and turbulent flow regimes. The numerical results agreed very well with the experimental data, and demonstrated that total thermal resistance (R_{th}) less than 0.1°C/(W/cm²) can be achieved, albeit with pressure drops in excess of 2.5 bar. Peng and Peterson [8,9] investigated experimentally the forced convective heat transfer and pressure drop for water flows in SRMs having hydraulic diameters between 0.133mm and 0.367 mm and water velocities between 0.2 and 12m/s. They created empirical heat transfer correlations for both the laminar and turbulent flow regimes which indicated that the geometric configuration of the MCHS (specifically the aspect ratio (H_{ch}/W_{ch}), hydraulic diameter (D_h), and ratio of hydraulic diameter and microchannel centre-to-centre distance (D_h/W_c)) were very influential.

Qu and Mudawar [10] conducted numerical investigation of the fluid flow and heat transfer in a rectangular MCHS similar to that used in the experimental work carried out by Kawano et al. [11]. They observed that the Nusselt number (Nu) and heat flux had much higher values in the region near the channel inlet due to the thin thermal boundary layer in the developing region, and its value varied around the channel periphery, approaching zero in the corners where the flow is weak. Heat sinks with rectangular [5,7-11], trapezoidal [12-14], triangular [15] and circular microchannels [16-18] have been studied extensively, however a small number of experimental studies have demonstrated that other novel shapes, including U-shaped [19], wavy [20,21], tortuous [22,23] and serpentine [24] channels, can offer attractive performance advantages. A number of other channel shapes such as zigzag, curvy and step-shaped channels have been investigated numerically by Mohammed et al. [25,26]. This showed that the heat transfer performance of these were superior to those of straight and wavy channels, with the zigzag channel having the highest friction factor and pressure drop penalty followed by the curvy and step-shaped channels. These studies have demonstrated that convective heat transfer in the laminar flow regime can be enhanced by inducing recirculating flow in the microchannels. For curved channels, the eddies generated by centrifugal forces can enhance mixing and the resultant convective heat transfer [21]. Recently Chen et al. [27] used numerical and experimental method to study thermal resistance (R_{th}) and pressure drop (ΔP) in a single path serpentine MCHS. By parametrising the MCHS using four design variables, namely, the number of channels, width of channel, height of channel and inlet flow velocity, they explored the dependence of both R_{th} and ΔP on these parameters.

This paper presents the first comprehensive experimental and numerical investigation of the thermal and hydraulic performance of water flows within DPSM and TPSM. The performance of two designs are compared experimentally and numerically with both of the conventional SRM and SPSM heat sinks in terms of ΔP, R_{th} and Nu, for a wide range of water flow rates. The paper is organised as follows: The MCHSs of interest, experimental apparatus and analytical techniques used to determine their heat transfer and flow characteristics are described in section 2. The conjugate heat transfer model is described in section 3 and a comprehensive series of experimental and numerical results is presented in section 4. Conclusions are drawn in section 5.

2. Experimental Methods

2.1. Experimental set-up and procedure

A schematic diagram of the main components of the experimental test rig is given in Fig. 1. Water from a 23 litre reservoir tank is driven through the flow loop using a miniature diaphragm water pump, passes through a flowmeter with constant flow rates ranging from $0.2 - 3.0 \, l/min$ and an inlet water temperature to the MCHS set to 20°C. The mass flow rate is controlled accurately by adjusting the pump speed by regulating the voltage and current supplied by a

DC-power supply and using a bypass flow loop and control valve. K-type sheathed thermocouples with 0.5 mm probe diameter were inserted into the inlet and outlet plenum of the test section to measure the water temperature at the microchannel inlet and outlet respectively. The total pressure drop between the inlet and outlet plenum of the MCHS models was measured using a digital pressure meter (model Comark C9555) having a range of 0 to 2.1 bar. Two power film resistors of resistance 20 Ω (MP9100 (TO-247)), mounted at the bottom of the MCHS, were used as a heat source with the maximum power reaching 100W for each one. The voltage and current input to the power film resistor heater was controlled by a DC power supply unit with an output range of 0-35 V and 0-4 A. Clear plastic tubes with an outer/inner diameter of 4mm/2.2mm and fittings were used to construct the flow loop. To minimise heat loss to the surrounding environment, the MCHS copper block was packed with insulating fibre glass, and then placed inside a clear, covered Acrylic Perspex plastic box having dimensions $(10 \times 10 \times 10)$ cm³.
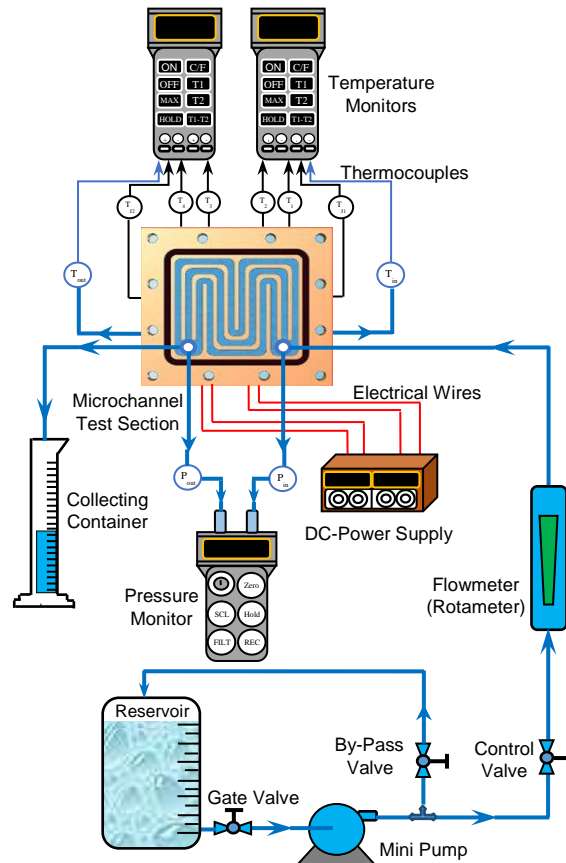

Fig. 1: Schematic diagram of experimental setup.

2.2. Design and fabrication of the MCHS test sections

Four different MCHSs were designed using SolidWorks [28] and manufactured using a high-accuracy Computer Numerical Control (CNC) milling machine (FANUC ROBODRIL). Copper was used as a material for the MCHS due to its high thermal conductivity of 388W/m.K at 20°C. The entire thickness (H) of the straight and serpentine MCHS designs was 5.5mm and 6.5mm respectively, while all the MCHSs had the same surface area of 45mm×41mm, the same base plate thickness (H_b) of 3.5mm and 12 parallel, rectangular microchannels with a 1mm wall thickness (W_w) between each microchannel. The microchannel base average surface roughnesses (ε) of all the MCHS models were measured using BRUKER-NPFLEX-LA 3D Surface Metrology System, and it was found to be $1.15 \pm 0.15 \mu m$. Around each microchannel top there is a groove made for an O-ring seal with a depth and width of 0.7mm and 1.5mm respectively to prevent water leakage.

[3]

The first MCHS test section had a series of parallel channels of rectangular cross section with width (W_{ch}), depth (H_{ch}) and length (L_{ch}) of 1mm, 2mm and 21mm respectively. The inlet and outlet manifolds of the MCHS were trapezoidal in shape and had tapered longitudinal sections for distributing the fluid flowing into and collecting fluid flowing out of the microchannels, as shown in Fig. 2. These manifolds were chosen to ensure that each channel had approximately the same mass flow rate of water. The other three MCHS test sections had a multi-serpentine rectangular cross section, referred to as the single path serpentine microchannel (SPSM), a double path serpentine microchannel (DPSM), and a triple path serpentine microchannel (TPSM), as illustrated in Fig. 3.
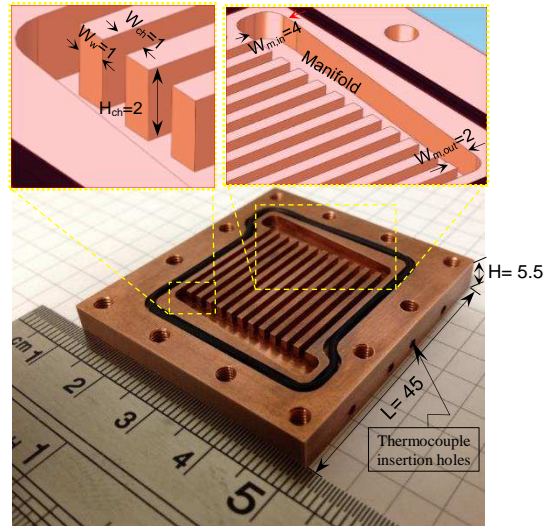
Fig. 2: Model and actual pictures of the straight rectangular MCHS design, all dimensions in mm.
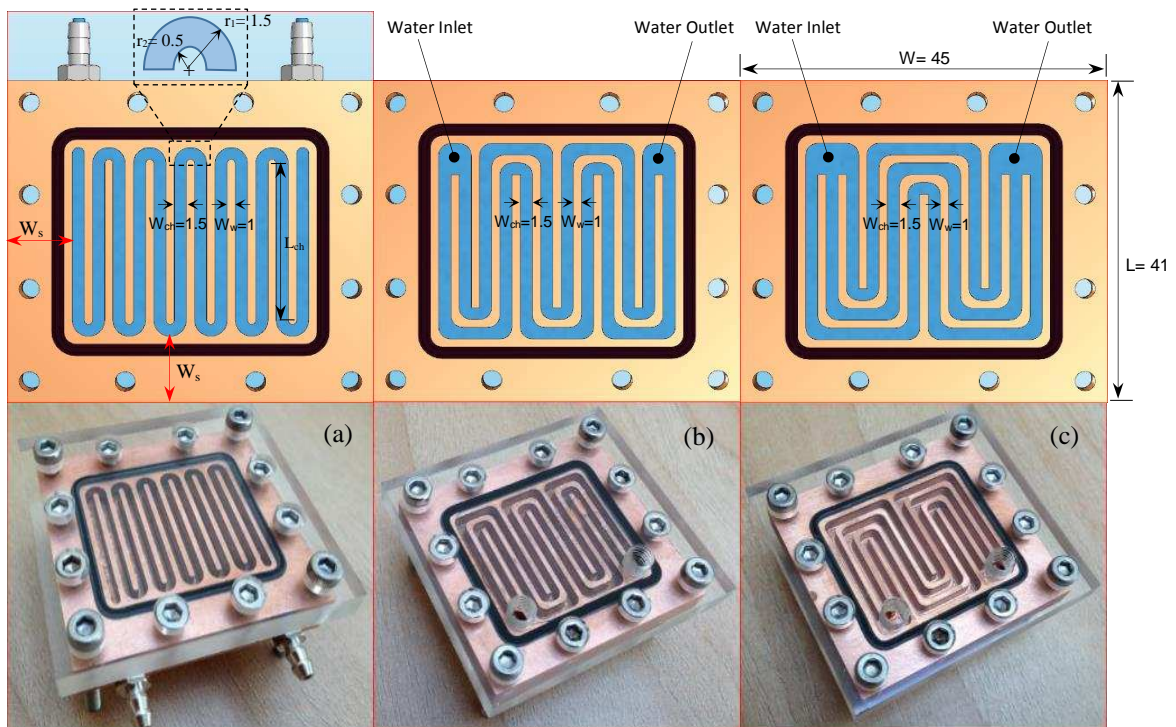
Fig. 3: Actual pictures and top view of (a) single, (b) double and (c) triple path multi-serpentine rectangular MCHS designs, all dimensions in mm.

Each MCHS was assembled with an Acrylic Perspex plastic sheet cover held onto the copper block by twelve stainless steel mounting screws (M3×0.5) and sealed with an O-ring. The force provided by the mounting screws was sufficient to seal the channels from the ambient environment and prevent water leakage to the outside of the MCHS models. Two 5mm circular through holes were drilled on the top side surfaces of the plastic covers and a male run tee union adapter

[4]

fixed on these threaded holes to create inlet and outlet water passages and to allow the inlet and outlet pressure to be measured, see Fig. 4. Two power film resistors were then permanently adhered on the bottom side of each MCHS test section using a thin consistent layer of thermal Ethoxy (Electrolube, TCER) with thermal conductivity of 2.2 W/m.K. The thickness of the thermal Ethoxy layer is measured manually for all the MCHS designs using a digital Vernier caliper, and was found to be $200\mu m \pm 6\mu m$.
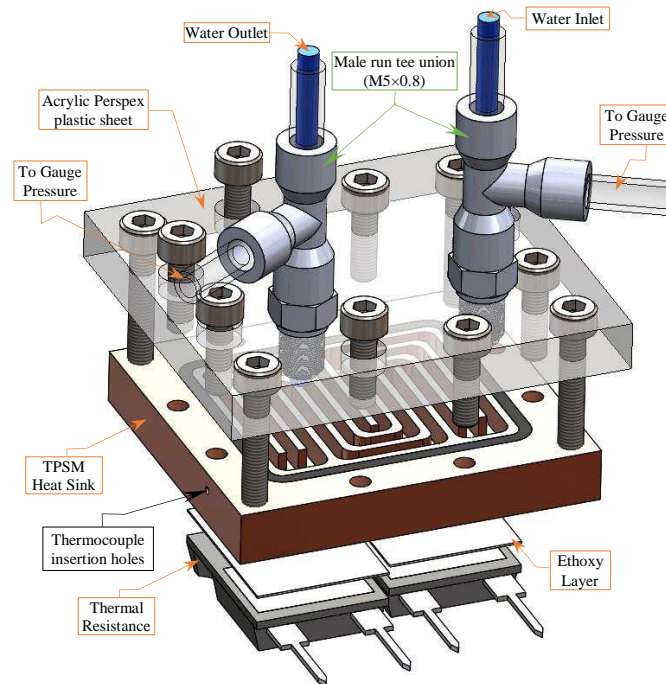

Fig. 4: Exploded view of triple path multi-serpentine MCHS model.

To record the maximum junction temperature of the resistor accurately, a small hole of diameter of 1mm was drilled from one side of the resistor until it reaches half the width of the resistor. In order to reduce the likelihood of defects to the thermal resistor and to bring a thermocouple as close to the junction temperature as possible, a gap of 0.25mm is left from the Nickel-Chromium (Ni-Cr) layer, see Fig. 5. A K-type thermocouple was inserted inside the bored hole in the heater surface located at the centre-line of the resistor, and the void filled with thermal Ethoxy material to prevent thermocouple movement and to fill the air-gap that existed between the hole and the thermocouple.
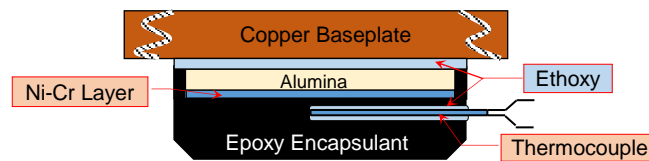
Fig. 5: Schematic diagram to measure the junction temperature.

To measure the wall temperature distribution along the MCHS sample, four K-type sheathed thermocouples with 0.5 mm probe diameter were inserted in the copper block at a distance of 1.75mm below the microchannel base until they reached half the width of the MCHS specimen. The locations of the thermocouple holes, as measured from the inlet of the MCHS and along its length are shown in Fig. 6. Thermal paste was used to fill the holes to ensure accurate temperature measurement.
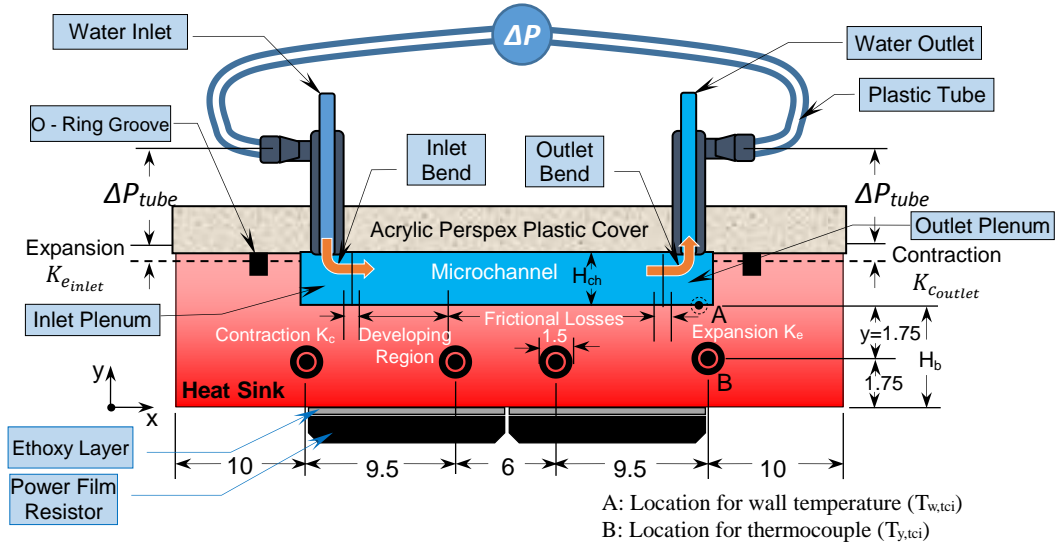
Fig. 6: Schematic representation for SRM design showing the thermocouple locations and pressure drop components, (All dimensions in mm).

2.3. Experimental measurements and data analysis

2.3.1 Heat loss measurements

Before conducting any experiments, the rate of heat loss dissipated from the MCHS specimen to the surroundings via natural convection, radiation and conduction was estimated. The maximum average heat loss was estimated to be approximately 8% of the input power from each model. This value was obtained from energy balance tests, where the enthalpy rise of the water flowing inside the MCHS test sections was compared with the electrical input power supplied to the heater. The steady-state sensible heat gain by the working fluid (Water) is given by:

$$q = \rho_f . Q_{in} . Cp_f \left(T_{f,out} - T_{f,in}\right) = V.I - q_{loss} = 0.92(V.I) \tag{1}$$

Where $T_{f,in}$ and $T_{f,out}$ are respectively the inlet and outlet water temperatures, which are obtained experimentally using the two thermocouples mounted upstream and downstream of the microchannels. The ρ_f and Cp_f are respectively the density and specific heat capacity of the water, which are determined based on the average of the fluid inlet and outlet temperatures $(T_{f,avg} = \left(T_{f,in} + T_{f,out}\right)/2)$. The V and I represent the voltage and current supplied to the heater by a DC-power supply device, respectively, while q_{loss} denotes the heat loss rate. The term Q_{in} (m³/sec) represents the volumetric flow rate of water which is measured with a flowmeter $(Q_{in} = n. V_{ch}. A_{ch})$, where V_{ch} denotes the water velocity in the microchannel, while n and A_{ch} respectively represent the number and cross sectional area of the microchannel $(A_{ch} = H_{ch} \times W_{ch})$, see Fig. 2.

2.3.2 Heat transfer analysis

The local heat transfer coefficient (h_x) and the average heat transfer coefficient (h_{avg}) can be calculated from Newton's law of cooling as:

$$h_x = \frac{q}{n . A_{eff}\left(T_{w,tci} - T_{f,x}\right)} \tag{2}$$

$$h_{avg} = \frac{q}{n . A_{eff}\left(T_{w,avg} - T_{f,avg}\right)} \tag{3}$$

[6]

The average channel base temperature can be obtained by ($T_{w,avg} = \sum_{i=1}^{4} T_{w,tci}/4$). Since direct measurement of the channel base temperature is difficult, it is determined by assuming one-dimensional steady state heat conduction between the thermocouple location (tci) and the microchannel base in the y direction. Accordingly, the local microchannel base temperature ($T_{w,tci}$) can be evaluated by:

$$T_{w,tci} = T_{y,tci} - \frac{y \cdot q}{A_h \cdot k_s} \tag{4}$$

where $T_{y,tci}$ represents the temperature closer to the microchannel base wall which was measured experimentally using a thermocouple, the subscript i denotes the location of the thermocouple used to measure the microchannel base temperature and A_h is the bottom heated area of the MCHS over which heating is provided by the resistors. In addition, k_s is the thermal conductivity of the heat sink material and y is the distance between the bottom wall of the microchannel and the thermocouple embedded to measure $T_{y,tci}$ as shown in Fig. 6. $T_{f,avg}$ and $T_{f,x}$ respectively denote the average fluid temperature and the local fluid bulk mean temperature at location x along the axial location of the channel:

$$T_{f,x} = T_{f,in} + \frac{x}{L_{ch}}\left(T_{f,out} - T_{f,in}\right) \tag{5}$$

In the experiments heat is transferred to the fluid through three microchannel walls only and the fourth wall (Top) is assumed to be adiabatic. Hence A_{eff}, the effective surface area available for convective heat transfer per microchannel, for the single straight rectangular microchannel can be calculated as:

$$A_{eff} = A_{base} + \eta_f . A_{fin} = L_{ch}\left(W_{ch} + 2H_{ch} \cdot \eta_f\right) \tag{6}$$

where A_{base} represents the bottom area for convection for each microchannel, A_{fin} corresponds to the area of one side wall for a single microchannel and L_{ch} denotes the microchannel length. The term η_f is defined as the fin efficiency assuming an adiabatic tip condition which is correlated by:

$$\eta_f = \frac{tanh(m.H_{ch})}{m.H_{ch}} \quad \text{where the fin parameter } (m) \text{ is given by} \quad m = \sqrt{\frac{2h}{W_w.k_s}}. \tag{7}$$

The effective heat transfer area of the single path multi-serpentine rectangular MCHS can be obtained by:

$$A_{eff} = \left(n. W_{ch}. L_{ch} + \frac{\pi}{2}(n-1)(r_1^2 - r_2^2) + 2r_1. W_{ch}\right) + \eta_f(2n. H_{ch}. L_{ch} + \pi H_{ch}(n-1)(r_1 + r_2) + 4r_1. H_{ch}) \tag{8}$$

where L_{ch} represents the length of the straight microchannel $\left(L_{ch} = L - 2(W_s + r_1)\right)$. The symbols r_1 and r_2 denote the outer and inner radius of the curved microchannel respectively, while W_s represents the outside wall thickness as shown in Fig. 3(a). For the SRM model A_{eff} =1260 mm², while for the SPSM, DPSM and TPSM models A_{eff} = 2143, 2124 and 2064 mm², respectively. The average Nusselt number (Nu_{avg}) of the fluid can be expressed as:

$$Nu_{avg} = \frac{h_{avg}. D_h}{k_f} \tag{9}$$

where k_f represents the fluid thermal conductivity which is evaluated at $T_{f,avg}$, and D_h denotes the microchannel hydraulic diameter $\left(D_h = \frac{4A_{ch}}{P_w} = \frac{2 (W_{ch} . H_{ch})}{W_{ch} + H_{ch}}\right)$.

2.3.3 Pressure drop analysis

A digital pressure gauge was used to measure the total pressure drop (ΔP_t) directly using two plastic tubes connected to the inlet and outlet of the MCHS plenum. The values of ΔP_t for the straight rectangular microchannel (SRM) heat sink can be obtained analytically by summing the major and minor pressure losses ($\Delta P_t = \Delta P_{ch} + \Delta P_{minor\ losses}$). The minor losses in the present work have eight components as depicted in Fig. 6. The first two components are due to flow of water inside the inlet and outlet tube of the male run tee union positioned on the top of the MCHS cover, while the third and fourth components are due to the 90 degree bends, K_{90}, that forms between the outlet of the tube and the inlet plenum (header) from the inlet side of the MCHS and the bend that forms between the outlet plenum and the tube inlet from the outlet side of the MCHS. The fifth and sixth pressure losses occur respectively due to the sudden expansion between the outlet tube and inlet plenum ($K_{e_{inlet}}$) and the sudden expansion between the microchannel exit and the outlet plenum (K_e). Similar pressure losses occur due to sudden contractions to give the last two pressure loss components, the first one was at the inlet plenum and microchannel inlet ($K_{c_{outlet}}$) and the second at the outlet plenum and the inlet tube (K_c).

The major component of the pressure drop (ΔP_{ch}) occuring in the core of the microchannels can be obtained by summing two components, the first component is due to the frictional factor in the developing region which occurs in the entrance region of the microchannel, while the second component is obtained in the fully developed region in the remaining length of the channel, as shown in Fig. 6. For the SRM heat sink, the total pressure drop (ΔP_{t_SRM}) between the inlet and outlet MCHS can be expressed as:

$$\Delta P_{t\_SRM} = \frac{\rho_f \cdot V_{ch}^2}{2}\left((2K_{90}) \cdot \left(\frac{A_{ch}}{A_p}\right)^2 + K_c + K_e + \frac{4f_{app} \cdot L_{ch}}{D_h} \right) + \left(\rho_f \cdot V_{tube}^2 \left(\frac{4f_{tube} \cdot L_{tube}}{D_{tube}} \right) \right) + \frac{\rho_f \cdot V_{tube}^2}{2}\left(\frac{A_{tube}}{A_P}\right)^2 \left(K_{e_{inlet}} + K_{c_{outlet}} \right) \qquad (10)$$

f_{app} refers to the apparent friction factor and accounts for the pressure drop due to friction and the developing region effects [29]. For developing laminar and turbulent flow regimes, f_{app} can be calculated by using correlation equations proposed by Shah [30] and Phillips [7] respectively, see Table 1 in the Supplementary Data (SD), section 1. The plenum area of the SRM heat sink design is 79.64mm², while the length and diameter of the inlet and outlet tube of the male run tee union are 25mm and 2.5mm, respectively. The loss coefficient of the sudden expansion ($K_{e_{inlet}}$) and the sudden contraction ($K_{c_{outlet}}$) can be predicted using the simple relationships found in Idelchik [31]:

$$K_{e_{inlet}} = \left(1 - \frac{A_{tube}}{A_P} \right)^2 \qquad and \qquad K_{c_{outlet}} = 0.42\left(1 - \frac{A_{tube}}{A_P} \right) \qquad (11)$$

where A_{tube} and V_{tube} respectively represent the area ($\pi D_{tube}^2/4$) and velocity (Q_{in}/A_{tube}) of the male run tee union tube. Since the flow inside the tubes was found to be in the turbulent regime for most of the water flow rates used, the correlation equation offered by Phillips [7] can be used to evaluate the friction factor. The K_{90} denotes the bend loss coefficient associated with each of the 90° bends at the channel inlet and outlet and Phillips [7] recommended $K_{90} \approx 1.2$. Whereas K_c and K_e respectively represent the contraction and expansion loss coefficients due to area changes which are based on the ratio of the channel area to the plenum flow area (A_{ch}/A_P) and the flow regime (laminar or turbulent), their values can be estimated from the graphical information given for a square channel by Kays and London [32].

With regard to the SPSM with n channels and a total $n - 1$ fins (U-bends), see Fig. 3(a), the total pressure drop is caused by two components, namely pressure drop due to straight channel friction and U-bends. Thus, the total pressure drop for the MCHS can be written in general form following [33]:

[8]

$$\Delta P_t = \frac{1}{2} \cdot \rho_f \cdot V_{ch}^2 \left(4 f_{app} \cdot \frac{L_t}{D_h} + \sum_{i=1}^{n-1} \xi_i \right). \tag{12}$$

The symbol ξ_i represents the excess loss coefficient of bend i in the MCHS, and L_t denotes the total length of the channel (The length of both straight and bend channels based on mean radius of curvature of the bend). To calculate the value of the excess bend loss coefficient (ξ), Maharudrayya et al. [33] carried out numerical simulations of laminar single-phase flow through 180° bends and serpentine rectangular channels using CFD, and three-regime correlations proposed, see SD, section 3. Hence, the total pressure drop for SPSM can be simplified to be:

$$\Delta P_{t\_SPSM} = \frac{1}{2} \cdot \rho_f \cdot V_{ch}^2 \left(4 f_{app} \cdot \frac{L_{t.}}{D_h} + \sum_{i=1}^{n-1} \xi_i + K_c + K_e \right), \tag{13}$$

for the double path multi-serpentine rectangular microchannel (DPSM) design, the total pressure drop can be written as:

$$\Delta P_{t\_DPSM} = \frac{\rho_f \cdot V_{ch}^2}{2} \left(\frac{4 f_{app} \cdot L_t}{D_h} + \sum_{i=1}^{n-2} \xi_i + K_c + K_e + 2 K_{90} \left(\frac{A_{ch}}{A_p} \right)^2 \right) + \rho_f V_{tube}^2 \left(\frac{4 f_{tube} \cdot L_{tube}}{D_{tube}} \right) + \frac{\rho_f \cdot V_{tube}^2}{2} \left(\frac{A_{tube}}{A_P} \right)^2 \left(K_{e_{inlet}} + K_{c_{outlet}} \right) \tag{14}$$

and the total pressure drops for a triple path multi-serpentine rectangular microchannel (TPSM) design can be expressed by:

$$\Delta P_{t\_TPSM} = \frac{\rho_f \cdot V_{ch}^2}{2} \left(\frac{4 f_{app} \cdot L_t}{D_h} + \sum_{i=1}^{n-3} \xi_i + K_c + K_e + 2 K_{90} \left(\frac{A_{ch}}{A_p} \right)^2 \right) + \rho_f V_{tube}^2 \left(\frac{4 f_{tube} \cdot L_{tube}}{D_{tube}} \right) + \frac{\rho_f \cdot V_{tube}^2}{2} \left(\frac{A_{tube}}{A_P} \right)^2 \left(K_{e_{inlet}} + K_{c_{outlet}} \right). \tag{15}$$

The Fanning friction factor (f_F) was utilized in this work. It is defined as the ratio of wall friction forces to inertia forces and the f_F in rectangular microchannels can be rewritten as:

$$f_{ch} = \frac{2\tau_w}{\rho_f \cdot V_{ch}^2} = \frac{\Delta P_{ch} \cdot D_h}{2\rho_f \cdot L_{ch} \cdot V_{ch}^2} = \frac{W_{ch}^3 \cdot H_{ch}^3 \cdot \Delta P_{ch}}{\rho_f \cdot L_{ch} \cdot Q_{in}^2 (W_{ch} + H_{ch})} \tag{16}$$

where τ_w denotes the wall shear stress. The f_F occurring inside the curved channel is given by:

$$f_{curve} = \frac{\Delta P_{ch} \cdot D_h}{2\rho_f \cdot L_{curve} \cdot V_{ch}^2} = \frac{180}{\pi \cdot R_c \cdot \theta} \times \frac{W_{ch}^3 \cdot H_{ch}^3 \cdot \Delta P_{ch}}{\rho_f \cdot Q_{in}^2 (W_{ch} + H_{ch})} \tag{17}$$

where θ and R_c are respectively the angle of the channel (in degrees) and radius of curvature, while L_{curve} represents the length of the curved channel ($L_{curve} = \frac{\pi \cdot R_c \cdot \theta}{180}$).

2.4. Experimental uncertainty

In the present work, the ASME standard [34] and the Root-Sum-Square (RSS) method described by Coleman and Steele [35] were used to estimate the experimental uncertainties, U. In the experiments, an electronic digital Vernier caliper is used to measure various geometric dimensions of the MCHS test sections. Uncertainties for various critical parameters are tabulated in Table 3 in SD, section 2.

3. Mathematical model

3.1 Governing equations

Three-dimensional, steady, single-phase water flow and heat transfer in the MCHSs is modelled by assuming the flow is incompressible and that the effects of radiation and natural convection are negligible. Flow is modelled using the following continuity and Navier-Stokes momentum equations:

$$\nabla \cdot \mathbf{u} = 0 \qquad \text{(continuity equation)} \tag{18}$$

$$\rho_f (\mathbf{u} \cdot \nabla) \mathbf{u} = \nabla \cdot \left[-p \mathbf{I} + \mu_f (\nabla \mathbf{u} + (\nabla \mathbf{u})^T) \right] + \mathbf{F} \qquad \text{(momentum equation for laminar flow)} \tag{19}$$

[9]

$$\rho_f(\mathbf{u}.\nabla)\mathbf{u} = \nabla \cdot \left[-p\mathbf{I} + (\mu_f + \mu_T)(\nabla\mathbf{u} + (\nabla\mathbf{u})^T) - \frac{2}{3}\rho k\mathbf{I} \right] + \mathbf{F} \qquad \text{(momentum equation for turbulent flow)} \qquad (20)$$

Eqs. (19 and 20) are the momentum equations for steady and incompressible for both laminar and turbulent flow regimes. $\mathbf{u}$ and p are respectively the fluid velocity vector and the fluid pressure (Pa). The term $\mathbf{F}$ is the body force per unit volume (N/m^3) and $\mathbf{I}$ denotes the unit diagonal matrix. The Reynolds number in the tube can be calculated by ($Re = \frac{\rho_f.V_{tube}.D_h}{\mu_f}$) and both laminar and turbulent cases are considered. In the present study the standard k-ω turbulence model has been used [36,37] to provide a robust and accurate model. The k-ω model introduces two additional variables: the turbulent kinetic energy, k (m^2/s^2), and specific dissipation rate, ω ($1/s$). The transport equations for k and ω that used in the CFD model are based on those given by Wilcox [38]:

$$\rho(\mathbf{u}.\nabla)k = \nabla \cdot [(\mu + \mu_T\sigma_k^*)\nabla k] + P_k - \rho\beta_o^*\omega k \qquad (21)$$

$$\rho(\mathbf{u}.\nabla)\omega = \nabla \cdot [(\mu + \mu_T\sigma_\omega)\nabla\omega] + \alpha\frac{\omega}{k}P_k - \rho\beta_o\omega^2 \qquad (22)$$

The production term and the turbulent viscosity are defined by:

$$P_k = \mu_T[\nabla\mathbf{u}:(\nabla\mathbf{u} + (\nabla\mathbf{u})^T)] , \qquad \mu_T = \rho\frac{k}{\omega} \qquad (23)$$

while the empirical turbulent model constant parameters are ($\alpha = \frac{13}{25}, \sigma_k^* = \frac{1}{2}, \sigma_\omega = \frac{1}{2}, \beta_o = \frac{9}{125}, \beta_o^* = \frac{9}{100}$).

The heat transfer (energy) equations for the liquid and the solid can be expressed respectively as:

$$\rho_f C_{p_f}\mathbf{u}.\nabla T = \nabla \cdot \left((k_f + k_T)\nabla T \right) + Q \qquad (24)$$

$$\nabla \cdot (k_s\nabla T) = 0 \qquad (25)$$

where C_{p_f} and k_f denote the specific heat and thermal conductivity of the fluid respectively, Q represents the internal heat generation (W/m^3) and k_s represents the thermal conductivity of the solid (heat sink). k_T is the turbulent thermal conductivity $\left(k_T = \frac{\mu_T.C_{p_f}}{Pr_T} \right)$, and Pr_T is the turbulent Prandtl number (using Kays- Crawford [39]). The above flow and heat transfer equations are solved using COMSOL Multiphysics version 5.2.

3.2 Boundary conditions:

The computational domain and boundary conditions used are highlighted in Fig. 7. Except at the bottom of the MCHS, all the outer surface boundaries are considered to be adiabatic. Heating power was supplied at the bottom surface of the MCHS using two resistance heaters via ($-\boldsymbol{n}.(-k\nabla T) = q/A_h$), where the term $\boldsymbol{n}$ denotes the outward normal vector on the boundary of the domain. A thin layer of Ethoxy, with thickness (d_l) of 200 μm and thermal conductivity (k_l) of 2.2 W/(m.K), was mounted between the heater and the base of the heat sink. There is no internal heat generation in the MCHS, so $Q = 0$ there, see Eq. (24).
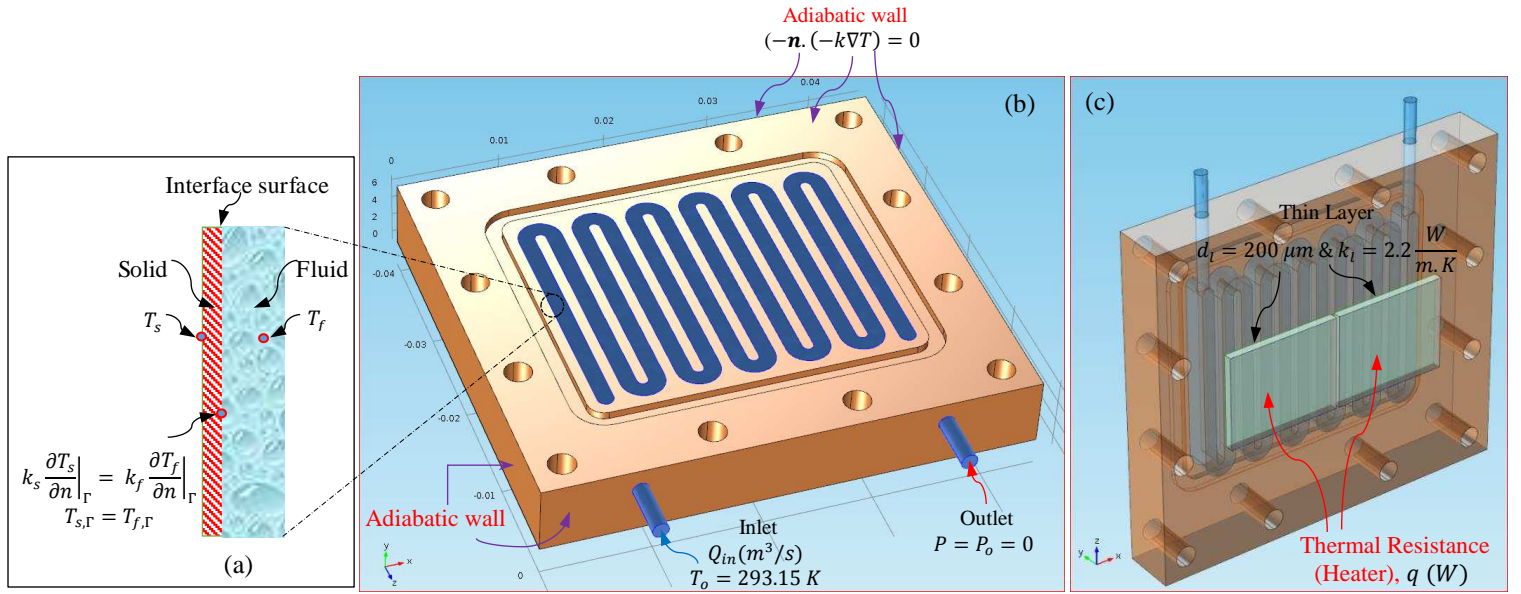
Fig. 7: 3-D view and back side of SPSM design used in simulation to explain the boundary conditions; a) Conjugate heat transfer of the MCHS; b) Isometric view; c) Bottom side of the MCHS..

No-slip velocity boundary conditions $\mathbf{u_s} = 0$ are used at solid walls and wall temperatures are defined by $T_s = T_{f\ at\ wall}$. At liquid-solid boundaries the heat conduction and convective heat transfer to the fluid are coupled by imposing heat flux continuity at the interface between the fluid and the solid walls [10] as shown in Fig. 7(a) , where $T_{s,\Gamma}$ and $T_{f,\Gamma}$ are respectively the interface temperature for solid and liquid.

4. Results

4.1 Effect of Grid Refinement

The effects of grid density on the numerical solutions for all MCHS models were tested using four different mesh sizes, as indicated in Table 4 in SD, section 4, where grid 1 is the coarsest and grid 4 the finest for each particular MCHS model. The predicted values of the temperature between the heater and the heat sink bottom ($T_{junction}$) and average Nusselt number (Nu_{avg}) for all MCHS models for a water flow rate of $0.15\ l/min$, water inlet temperature set at 20°C and input power of 100W are given in Table 4. The deviation percentages, E, are calculated with respect to the solutions on grid 4 in each case; these are small (~2%), thus grid 3 is employed for all MCHS computations reported below as a suitable compromise between efficiency and accuracy.

4.2 Numerical Validation

The numerical model was validated against a number of previous, relevant studies. The first comparison is with the numerical and experimental results obtained by Qu and Mudawar [10] and Kawano et al. [11] respectively, who considered water flow in a single rectangular microchannel cooling a chip. The water inlet temperature is 20°C and a constant heat flux of 90W/cm² is supplied at the upper boundary. The silicon microchannels have a width and depth of 57μm and 180μm respectively, with a separating wall of 43μm. A free-tetrahedral mesh was used to simulate the single microchannel with 200,180 elements. The outlet thermal resistance ($R_{th,out} = (T_{surf,max} - T_{f,in})/q$) was determined over the Reynolds number range $80 \le Re \le 400$. It is clear from Fig. 8 that the predictions of $R_{th,out}$ agree well with the previous studies: a maximum discrepancy $< 3.5\%$ with Qu and Mudawar's [10] numerical predictions and $< 6.5\%$ with the experimental study of Kawano et al. [11].

[11]
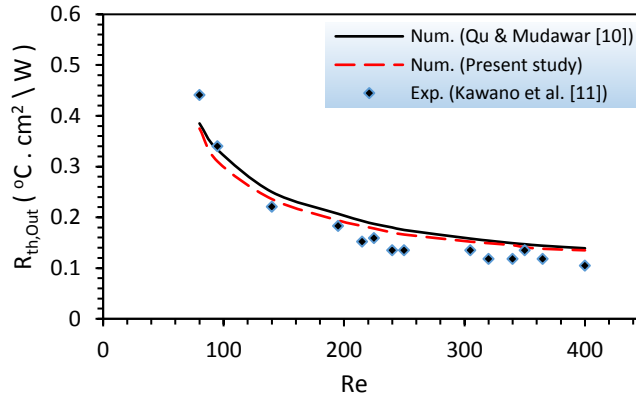
Fig. 8: Comparison between the numerical present work and Kawano et al. and Qu & Mudawar works for outlet thermal resistance.

4.3 Flow and pressure drop characteristics of MCHS

Fig. 9 shows the effect of water flow rate ($0.1 \leq Q_{in} \leq 1.0 \; l/min$) on the experimental measurements of the total pressure drop (ΔP_t) for the SRM heat sink with input heating powers of 50, 75 and 100W. Depending on the inlet tube diameter (2.5mm), the flow is considered turbulent when $Q_{in} \geq 0.15 \; l/min$. As expected, ΔP_t increases rapidly with flow rate and as the input power increases the pressure drop decreases monotonically. The latter behaviour is due to the reduction in density and viscosity, and this behaviour in unaffected by whether the water flow is in the laminar or turbulent flow regime. The experimental data for the heating power of 100W is also compared against analytical equation proposed (see, Eq. 10) and corresponding numerical predictions which simulate the entire SRM heat sink. As shown in Fig. 10, there is reasonable agreement between experimental data and with both the numerical and analytical predictions, with a typical discrepancies of 9% and 15%, respectively.
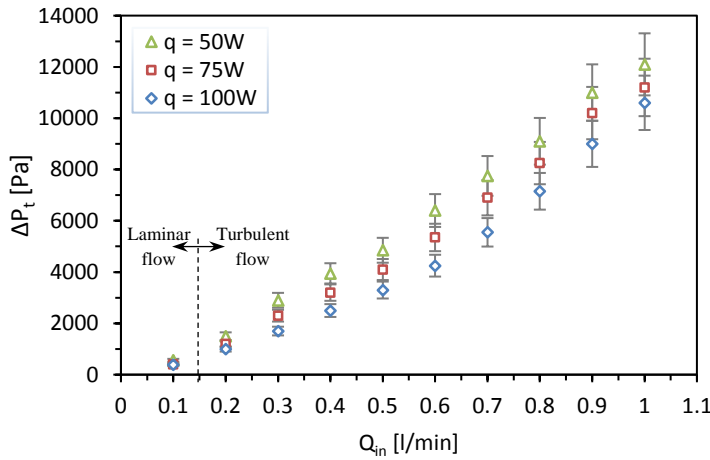

Fig. 9: The experimental total pressure drop in SRM heat sink design versus volumetric flow rate (Q_{in}) at three different input powers of 50, 75 and 100W.
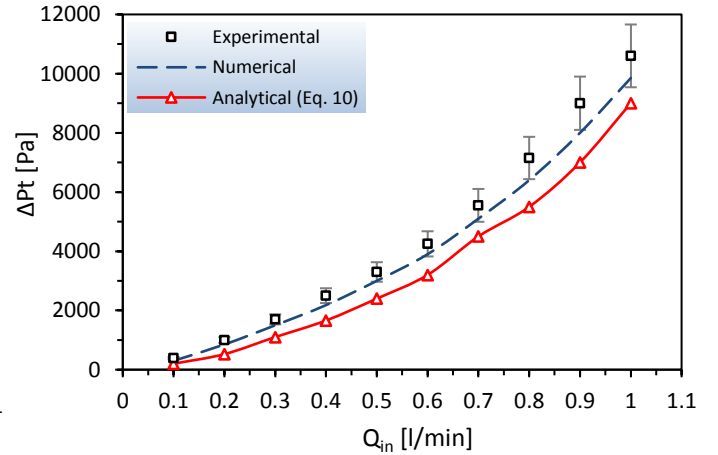

Fig. 10: Comparison for total pressure drop in SRM heat sink design versus volumetric flow rate (Q_{in}) at input power of 100W.

Fig. 11(a) compares experimental measurements and numerical predictions of ΔP_t versus Q_{in} for the SPSM design, while Fig. 11(b) shows the corresponding data for both the DPSM and TPSM test sections. The inlet tube diameter for the SPSM was 1.5mm, and 2.5mm for both the DPSM and TPSM. In all cases, as Q_{in} is increased ΔP_t increases rapidly due to both the larger friction forces generated inside the straight and curved channels and increases to the minor pressure losses. It is clear from the Fig. 11 that the SPSM has a higher pressure drop compared with the other MCHSs, while the second and third highest pressure drop were seen in the DPSM and TPSM, respectively. The maximum discrepancy between the experimental data and numerical predictions were found to be 12.5%, 10.6% and 10.2% for the SPSM, DPSM and TPSM designs, respectively.
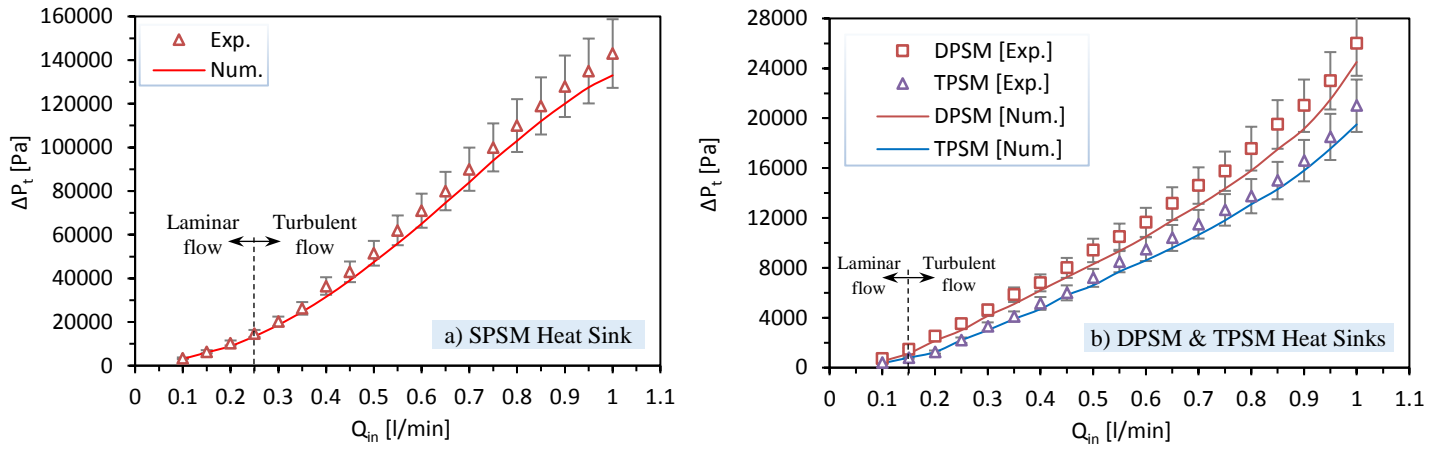
Fig. 11: The total pressure drop for (a) SPSM; (b) DPSM and TPSM models at different water flow rate and at input power of 100W.

The pressure distributions through the twelve-serpentine microchannels are illustrated in Fig. 12(a), while Fig. 12(b) demonstrates the percentage of pressure drop in both straight and bend microchannels in SPSM heat sink design at three different volumetric flow rate at input power of 100W. The markers in Fig. 12(a) represent maximum and minimum pressure in each straight portion of the microchannels, while the gaps between adjacent markers denote the pressure loss at bend, see Eqs. S.12 and S.13 in SD in section 3. The bend loss coefficient, ξ, is determined based on the correlation equation proposed by Maharudrayya et al. [33] for laminar single phase flow. The results obtained from the latter two equations were validated with numerical predictions and good agreement was achieved with average discrepancy of 8% for three different Q_{in}. As shown in Fig. 12(b) the percentage of pressure drop in bends were higher than those in straight channels at each Q_{in}, and this percentage increases with Q_{in}. The data obtained from Eq. (13) have been compared with experimental pressure drop and acceptable agreement was found, with typical discrepancy of 13% at each Q_{in}.
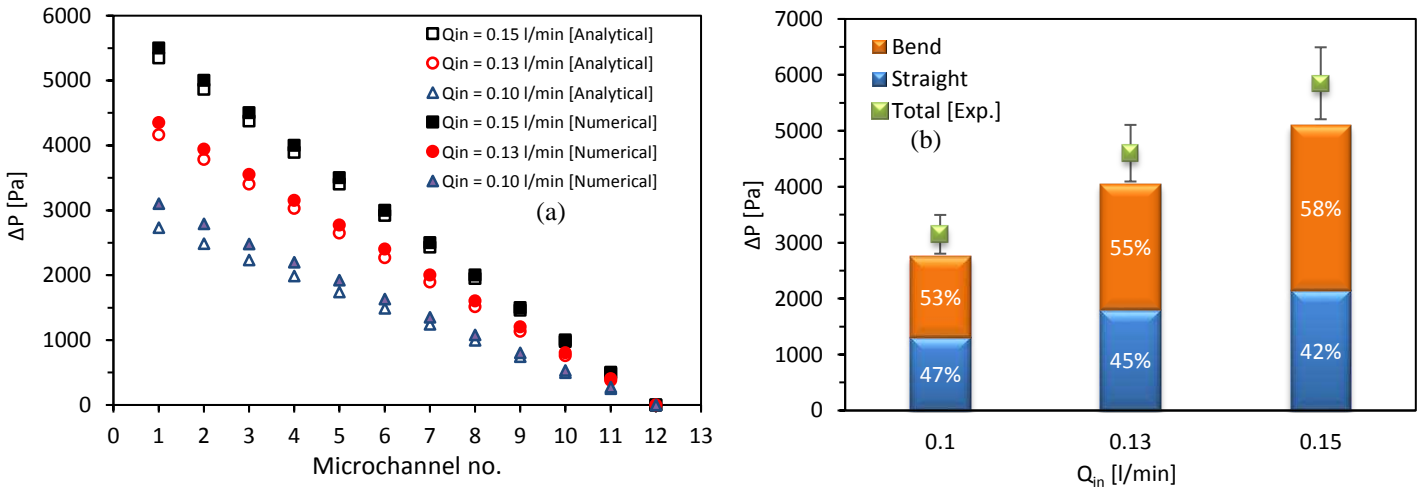
Fig. 12: The total pressure drop in SPSM design at different water flow rate and at input power of 100W; (a) pressure distribution through 12-serpentine channels ; (b) pressure drop percentage.

In the experiments the relative surface roughness (ε/D_h) for the four MCHS test sections was measured to be 0.875×10^{-3} for the SRM heat sink and 0.58×10^{-3} for the other three serpentine MCHS designs. Kandlikar et al. [40] studied the effect of surface roughness on pressure drop and heat transfer characteristics in 0.62 and 1.067 mm diameter stainless steel micro-tubes. The relative surface roughness for the larger diameter tube ranged from 0.00176 to 0.0028, and their results showed that the effects of varying surface roughness on pressure drop and heat transfer were insignificant. Since the relative roughnesses of the microchannels tested in the present experimental work were smaller than those of

[13]

Kandlikar et al. [40], it is likely that the surface roughness (ε) does not have a significant effect on the pressure drop and heat transfer coefficient in the present study.

Fig. 13 shows the pressure drop contours of the four MCHS designs used at the mid-depth plane of the channel (Z=H$_{ch}$/2) for laminar flow with $Q_{in} = 0.15 \ l/min$ and an input power of 100W. It can be seen that the SPSM creates a larger pressure drop than other cases. This is due to the facts that water in the SPSM flows inside one channel only, unlike the DPSM and TPSM where fluid is distributed into two and three microchannel respectively, leading to reductions in both the velocity and pressure drop in the latter two cases, and the larger microchannel length in the SPSM.
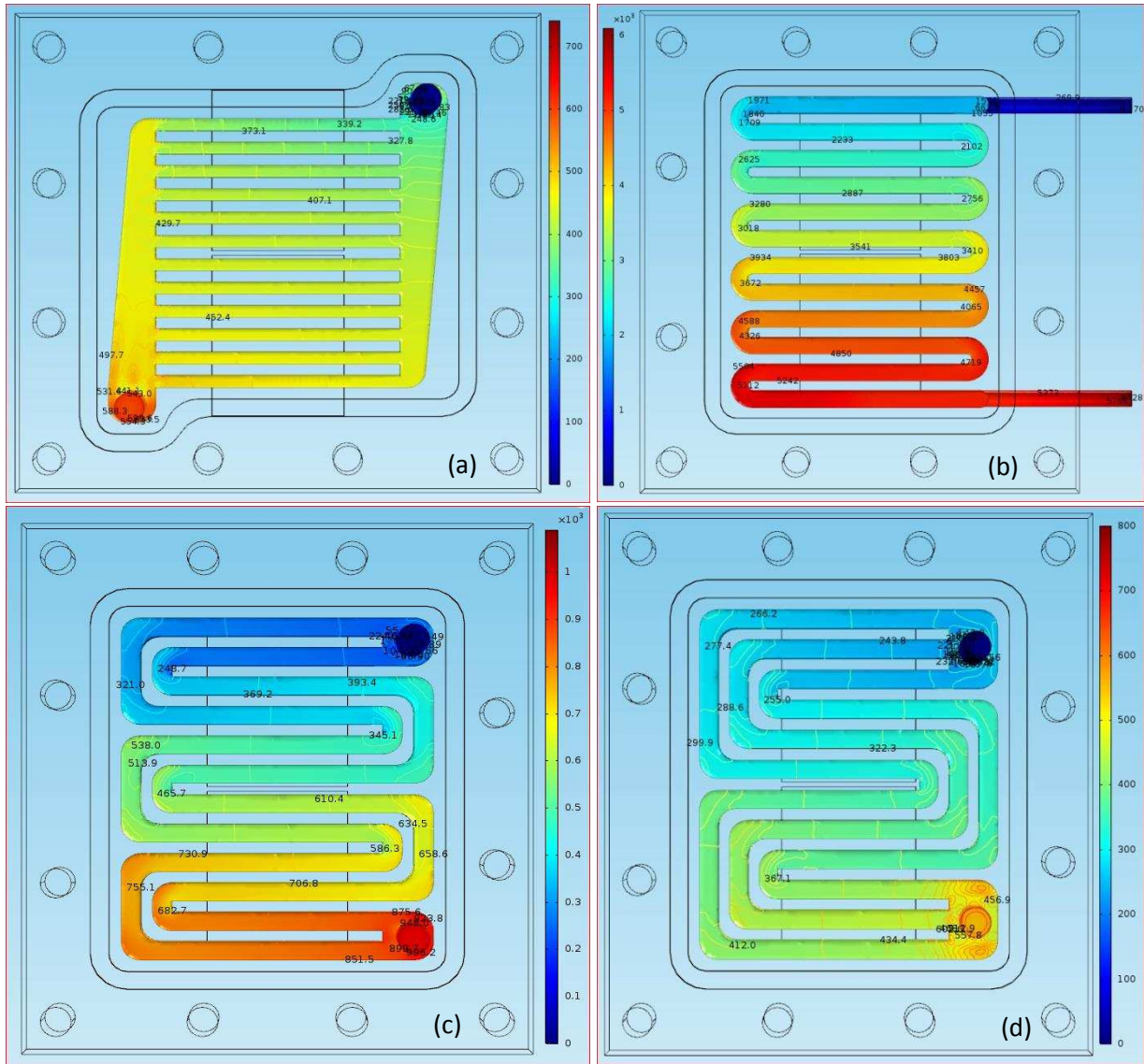
Fig. 13: Pressure drop contours of four MCHS at the mid-depth plane of the channel (Z=H$_{ch}$/2) : (a) SRM; (b) SPSM ; (c) DPSM; (d) TPSM.

4.4 Heat transfer characteristics of MCHS

4.4.1 Wall and fluid bulk temperature distribution

To obtain the heat transfer coefficient (h) and Nusselt number (Nu), the microchannel base and the fluid bulk temperature must first be determined. The local microchannel base temperature along the axial location of the microchannel can be calculated using Eq. (4) and the local fluid bulk temperature can be determined using Eq. (5). Fig. 14 presents experimental data and numerical predictions of the channel bottom temperature distribution along the microchannel length for the SRM test section, together with the inlet and outlet water temperatures measured using

[14]

thermocouples inserted at the inlet and outlet of the MCHS. Good agreement between theory and experiment was obtained, with discrepancies of less than 3.8% for the microchannel base temperature and 2.4% for the fluid bulk temperature.

The data shows how the microchannel base temperature increases along the flow direction and that the difference in temperature between the water and channel base along the axial flow direction is not constant which indicates that the flow is thermally developing throughout the whole of the MCHS, a desirable feature which leads to enhanced heat transfer.
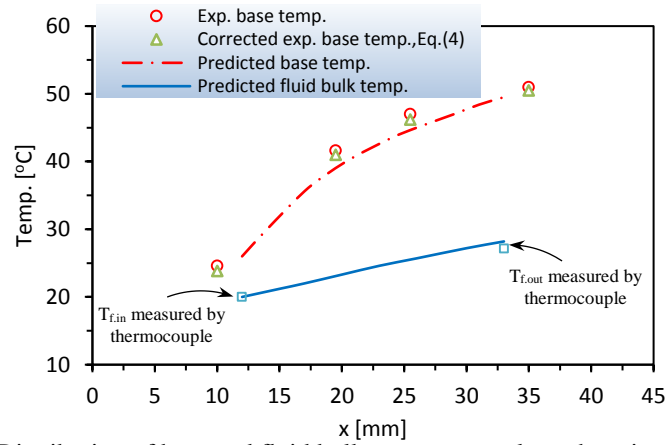

Fig. 14: Distribution of base and fluid bulk temperature along the microchannel axis distance for SRM design for $Q_{in} = 0.2\ l/min$ at input power of 100W.

4.4.2 Heat transfer coefficient (h) and the Nusselt number (Nu)

The length of the thermally developing entrance region was estimated using the equation proposed by Shah and London [41] ($L_{th} = x^*.Re.D_h.Pr$), where x^* denotes the dimensionless thermal entrance length, which is a function of the aspect ratio, and following Lee et al. [42] was taken to be 0.05 in this study. At an input power of 100W for the SRM heat sink, it was found that the thermally developing entrance length L_{th} exceeds the total microchannel length at every Re chosen, which indicates that the entire flow inside the channel is thermally developing.

After obtaining the average heat transfer coefficient (h_{avg}), the average Nusselt number (Nu_{avg}) can be calculated using Eq. (9), where the experimental values of h_{avg} are determined at $T_{f,avg}$ and $T_{w,avg}$ over a wide range of Q_{in} from 0.1 to 3.0 l/min. The experimental Nu_{avg} data obtained from the SRM design was compared with a number of correlation equations for both laminar and turbulent flow regimes as shown in Fig. 15. This shows that there is generally good agreement between the experimental measurements and numerical predictions of Nu_{avg} with an average discrepancy of less than 6% for both laminar and turbulent flow regimes.

The experimental Nu_{avg} data in the thermally developing laminar flow region are compared with the theoretical equation proposed by Lee and Garimella [43] for straight rectangular cross-section channels, for aspect ratios ranging between 1 and 10, (see Eq. (S.4) in the Table 2, SD, section 1). The equation of Lee and Garimella [43] is applicable to cases of uniform heat flux with circumferentially constant temperature and axially constant heat flux on the walls [29], and is valid when the dimensionless axial distance (x^*) is less than the length of the thermally developing region (x_{th}^*). Otherwise the flow is considered to be fully developed and Eq. (S.6) from Shah and London [41] will be used instead. The local average Nusselt number for three-sided heating can be estimated using the correction factor proposed by Phillips [7]:

[15]

$$Nu_{3,x}(x^*, \alpha) \approx Nu_{4,x}(x^*, \alpha) \cdot \frac{Nu_{3,fd\_lam}(\alpha)}{Nu_{4,fd\_lam}(\alpha)} \qquad (26)$$

where Nu_{3,fd_lam} and Nu_{4,fd_lam} denotes the Nusselt number in the fully developed region in the SRM for the three-sided and four-sided heating case respectively as defined in Eqs. (S.5 and S.6) in the Table 2, SD, section 1, while α is the aspect ratio ($\alpha = W_{ch}/H_{ch}$). It is clear from the Fig. 15 that there is good agreement between the experimental Nu_{avg} data obtained and the equation of Lee and Garimella [43] in the laminar flow regime for three sided wall heating, with a discrepancy of less than of 7%. These small differences in the Nu_{avg} values may be due to the fact that the flows in the present study feature both hydrodynamically- and thermally-developing flow, whereas Lee and Garimella's equation is for flow which is hydrodynamically fully developed but thermally developing. For turbulent flow ($Re >$ 3000), the experimental Nu_{avg} values for the SRM heat sink were compared with the experimental correlation proposed by Dittus-Boelter [44] for fully developed flow in smooth circular cross-sections, as given in Eq. (S.7) in the Table 2, SD, section 1. The maximum discrepancy in this case was around 12.5%.
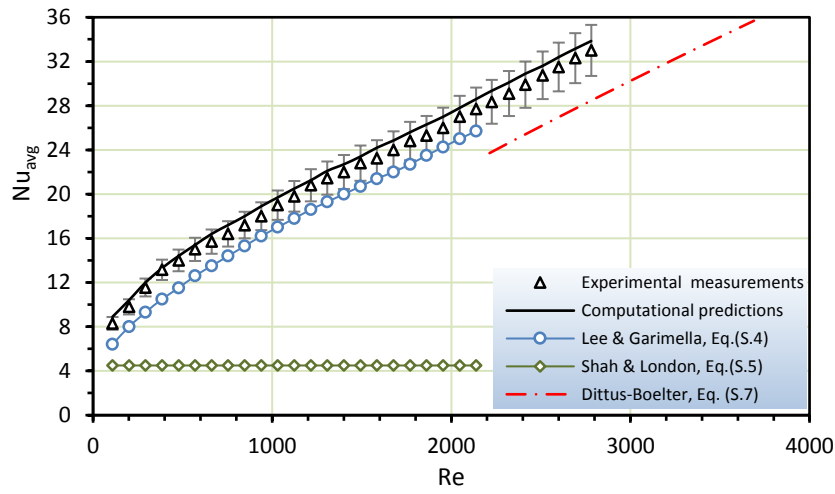
Fig. 15: The average Nusselt number versus Re for input power of 100W.

Fig. 16 compares the values of Nu_{avg} obtained experimentally and numerically as a function of flow rate, Q_{in}, for the four MCHS designs with an input heating power of 100W. The agreement between experiment and theory is once again reasonably good with average discrepancy of 6.5% for all MCHSs used, and all values of Nu_{avg} increase monotonically with Q_{in}. The Nu_{avg} values for the SPSM design, for the same Q_{in}, are the largest, followed by those for the DPSM and TPSM with those from the SRM the lowest. For example, at a volumetric flow rate is 0.5 l/min, Nu_{avg} for the SPSM is 18.9, which is 35.0%, 21.2% and 12.2% higher than the values for the SRM, TPSM and DPSM respectively. This due to the fact that the water in the SPSM and DPSM designs experiences a greater number of bends which disrupt the thermal boundary layer more effectively, reducing the wall temperature and leading to higher heat transfer. Note that, as seen above, this improved heat transfer for the SPSM and DPSM designs comes at the price of a significantly larger pressure drop compared to the other MCHS designs.

[16]
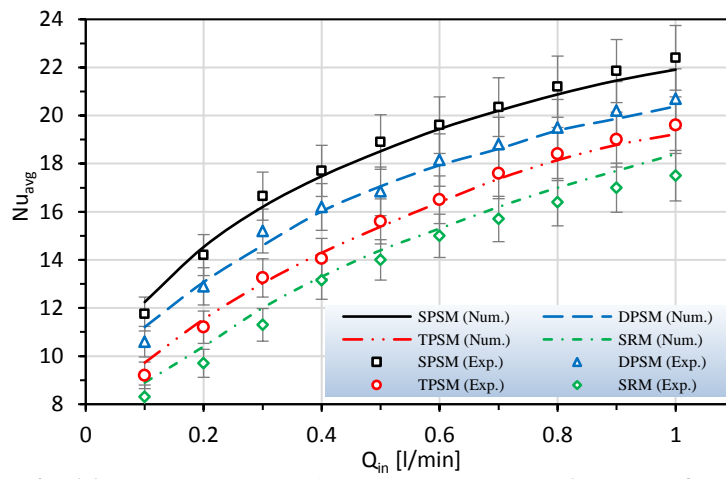
Fig. 16: The average Nusselt number versus water flow rate (Q_{in}) for four MCHS designs at input power of 100W.

Fig. 17(a-d) depicts the temperature contours for the four MCHS designs, which are taken at the half depth of the microchannel ($H_{ch}/2$), $Q_{in} = 0.15\ l/min$ and input power of 100W. For all MCHS, it can be noted that the temperature difference between the near wall fluid and core fluid increases as the flow travels downstream. The side wall temperature distribution of SPSM along the flow length was smaller than other MCHSs, while that for the SRM design was higher.
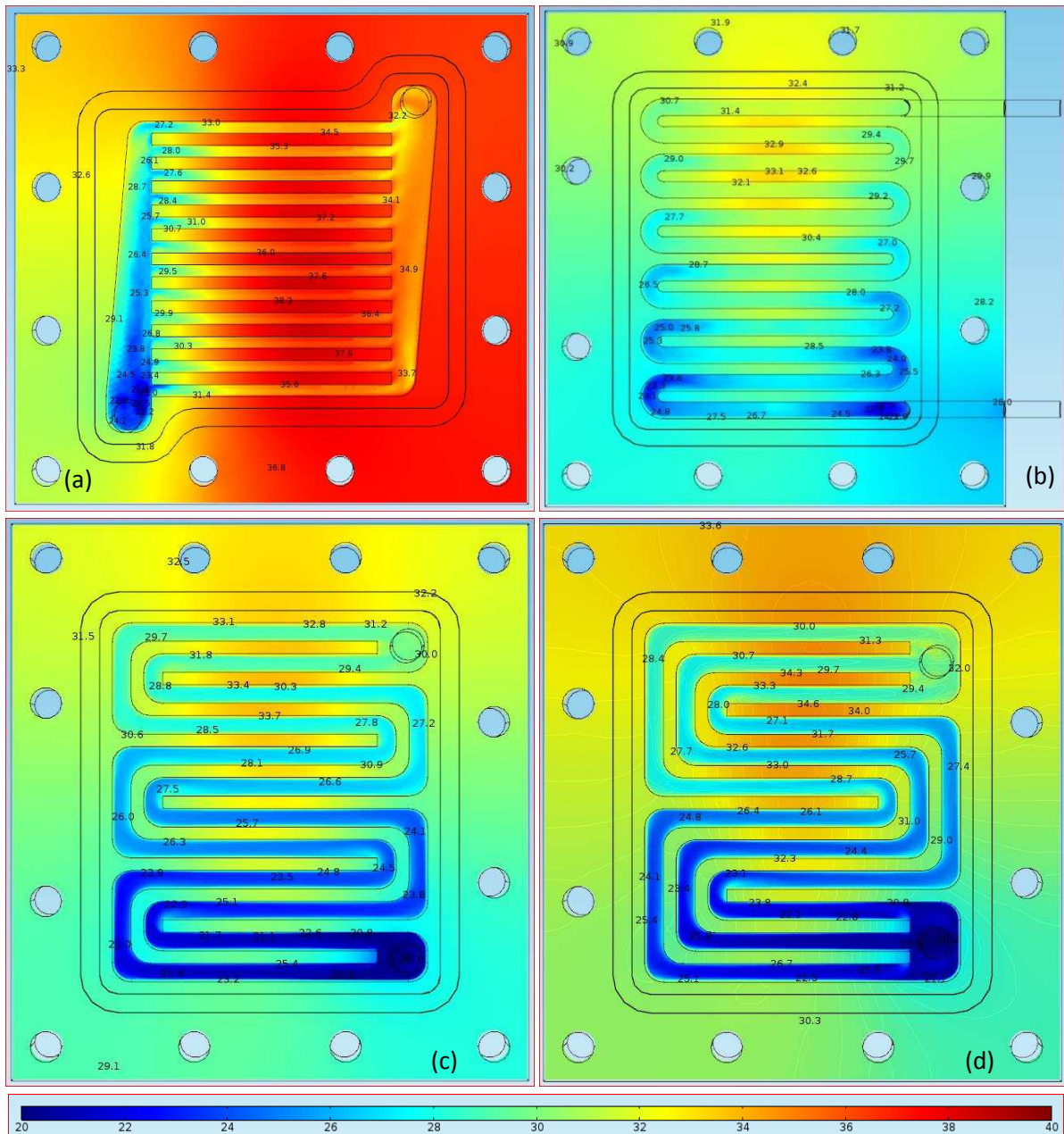
Fig. 17: Temperature contours of the four MCHSs: (a) SRM; (b) SPSM; (c) DPSM; (d)

[17]

Fig. 18 shows the velocity distribution and the velocity vectors for the SPSM test section, at the mid-depth plane of the channel ($H_{ch}/2$), for a volumetric flow rate (Q_{in}) of 0.15 l/min and an input power of 100 W. Due to flow continuity, the SPSM model has higher velocities compared with the other two types of serpentine channel designs, and it can be seen that a small region of recirculating flow is created near the inner surface of the bend, which aids the transportation of heat from the walls into water and disrupts the hydrodynamic and thermal boundary layers, thus improving the convective heat transfer [45].
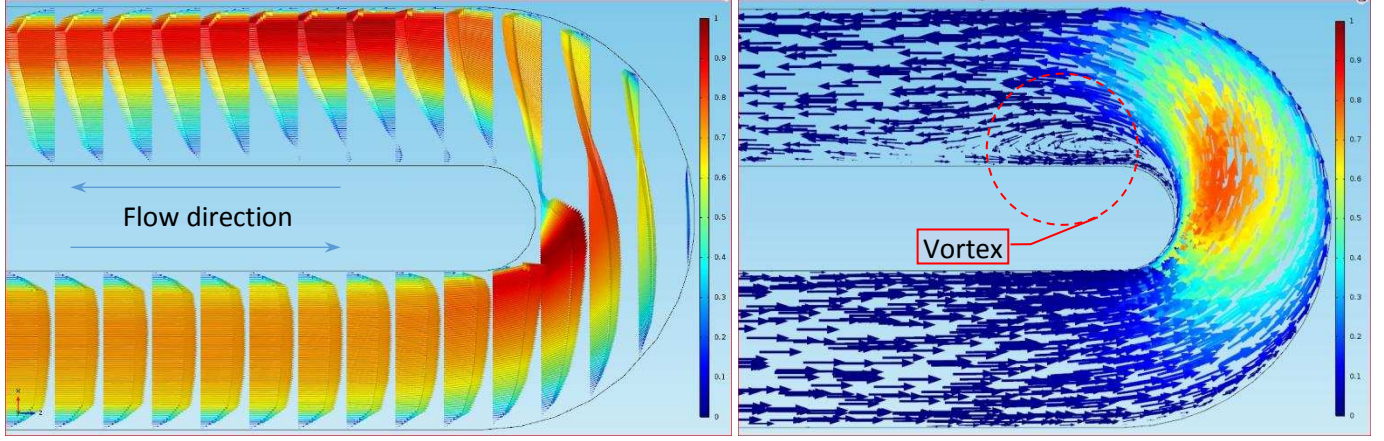

Fig. 18: Velocity distribution and velocity vectors for the SPSM design at $Q_{in} = 0.15\ l/min$ and input power of 100W.

4.5   Thermal resistance

The thermal resistance (R_{th}) measures the resistance of the MCHS to dissipating the input power [46], and is a commonly used parameter within the field of electronic cooling. It is defined by the ratio of the temperature difference of the substrate and the inlet of the microchannel to the heating power received by water in the microchannel region,

$$R_{th} = \frac{\Delta T}{q} = \frac{T_{max} - T_{f,in}}{q} \qquad (^{o}C/W) \tag{27}$$

where T_{max} is the maximum temperature measured by the four thermocouples inserted in the copper block (see Fig. 6), $T_{f,in}$ is the inlet water temperature, and $q(W)$ is the power supplied by the heater. Fig. 19 shows experimental measurements of R_{th} for the four different MCHS designs as a function of volumetric flow rate for an input heating power of 100W and an inlet water temperature of 20°C. The figure shows that the R_{th} values decrease for higher flow rates and those for the SPSM design are the smallest followed by the DPSM, TPSM and the conventional SRM. For example, at a $Q_{in} = 1.0\ l/min$, R_{th} for the SPSM is 0.1 °C/W, which is 32.8%, 26.2% and 13.7% lower than the values for the SRM, TPSM and DPSM respectively. The reasons for the smaller thermal resistances of the SPSM design have been described above, namely the preservation of hydrodynamically- and thermally-developing flow due to its multiple bends and the recirculating regions induced near the inner bend surfaces.
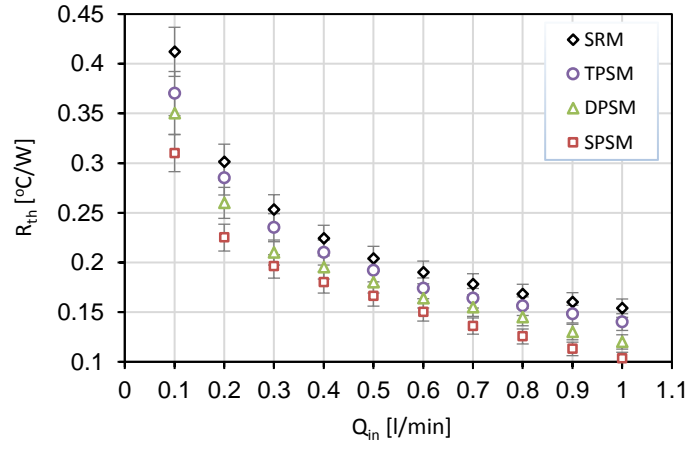
Fig. 19: Experimental total thermal resistance versus volumetric flow rate at input power of 100W.

4.6 Performance Evaluation Analysis

As indicated by the above experimental and numerical results for fluid flow and heat transfer, the SPSM heat sink designs can enhance heat transfer at the expense of a higher pressure drop. Thus, the benefits and disadvantages of the new serpentine MCHSs are assessed using a performance evaluation criterion (PEC) index based on the same pumping power consumption, as defined in [47, 48]:

$$PEC = \frac{E_{Nu_{avg}}}{\left(E_f\right)^{1/3}} = \frac{\frac{Nu_{avg}}{Nu_{avg,SRM}}}{\left(\frac{f}{f,SRM}\right)^{1/3}} \tag{28}$$

where $E_{Nu_{avg}}$ and E_f are respectively the heat transfer enhancement and friction factor parameters, which are defined as the average Nusselt number (Nu_{avg}) and friction factor (f) of the present enhanced MCHSs (SPSM, DPSM and TPSM) divided by those of SRM heat sinks, respectively. To calculate the f values for the three different serpentine MCHS configurations, Eqs. (13, 14 and 15) were used to determine the apparent friction factor (f_{app}) since the total pressure drop and the minor pressure losses are known, while Eq. (10) was used to estimate the f_{app} for the SRM heat sink. The PEC values of all the MCHS designs are plotted as functions of volumetric water flow rate (Q_{in}) as shown in Fig. 20. It is observed that the PEC of the SPSM heat sink is the smallest. This implies that the SPSM requires higher pumping power to achieve a higher heat transfer coefficient, while the PEC of the TPSM heat sink is the highest which implies that the higher thermal performance is achievable with less pumping power.

In addition, it can be seen that the values of PEC are decreased when $Q_{in} > 0.2 \; l/min$ for all MCHS test sections, and this due to the high pressure drop penalty which outweighs the heat transfer enhancement ($E_{Nu_{avg}}$) especially in the SPSM heat sink. It should be noted that the PEC values for both DPSM and TPSM designs are larger than 1 compared with the SPSM which is around 0.71, and this belong to the high pressure drop penalty for the SPSM design although the increase in the $E_{Nu_{avg}}$.

[19]
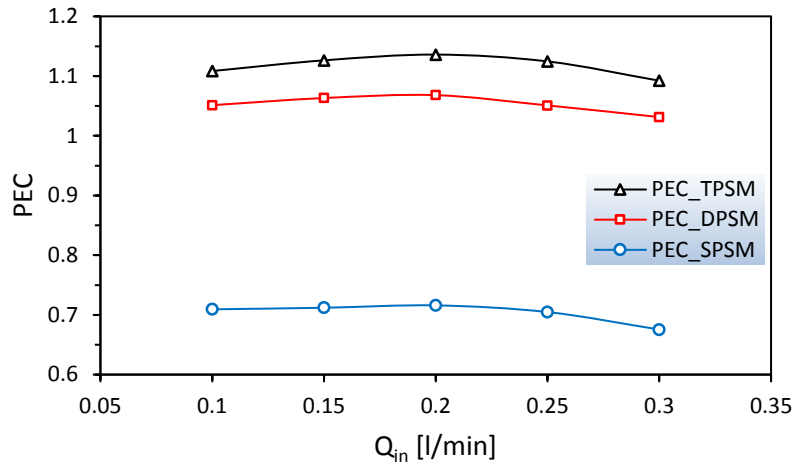
Fig. 20: Performance evaluation criterion obtained from experiments for three serpentine MCHS designs versus Q_{in} at input power of 100W.

5. Conclusions

This study has demonstrated that channel design in MCHS has a strong influence on both heat transfer and pressure drop. Experimental and numerical results show that Nu_{avg} increases monotonically with flow rate, due to reductions in the thickness of the thermal boundary layer, and that the SPSM design provides the most effective heat transfer, followed by the DPSM and TPSM with the SRM heat sink having the poorest heat transfer. The experiments show further that this leads to the SPSM design having the smallest thermal resistances, with values typically third of those for the poorest performing, SRM heat sink.

The numerical predictions of Nu_{avg} agree well with the experimental measurements with an average discrepancy of around 6% for both the laminar and turbulent flow regimes. Comparisons with existing correlations for Nu_{avg} for SRM show that the present experimental results agree well with the correlation of Lee and Garimella [43] in the laminar regime, with a discrepancy of less than 7%, and with that of Dittus-Boelter [44] in the turbulent regime, with a discrepancy of around 12.5%. The numerical solutions show that the channel bends are very influential in preventing the hydrodynamic and thermal boundary layers attaining a fully-developed state and that their greater influence for the SPSM and DPSM designs leads to enhanced heat transfer compared to the other designs. In the SPSM case, the numerical results also reveal the presence of a recirculating flow region that further enhances heat transfer from the inner bend wall.

These improvements in heat transfer are, however, achieved at the price of significantly larger pressure drops for the SPSM design, the values of which are reduced by the smaller water density and viscosity at high heating power densities. Practical design considerations, where the goal is to achieve a high heat transfer without excessive pressure drop, leads to a multi-objective design optimisation problem. This design optimisation will be addressed in future work.

Appendix A. Supplementary data

Supplementary data associated with this article can be found, in the online version, at http://

[20]

Nomenclature

A_{base}	Base area of channel [m²]	$T_{w,tci}$	Channel base temperature at thermocouple location (i = 1–4), [°C]
A_{ch}	Cross-sectional area of channel [m²]	$T_{f,out}$	Outlet fluid temperature [°C]
A_{eff}	Effective heat transfer area per channel [m²]	$T_{f,in}$	Inlet fluid temperature [°C]
A_{fin}	Surface area of fin [m²]	$T_{f,x}$	Local fluid bulk temperature [°C]
A_h	Bottom heated area of the MCHS [m²]	$T_{f,avg}$	Fluid bulk temperature [°C]
A_P	Plenum area [m²]	$T_{w,avg}$	Average channel base temperature [°C]
Cp_f	Specific heat of fluid [J/kg.K]	V	Voltage [V]
D_h	Hydraulic diameter [m]	V_{ch}	Velocity in microchannel [m/s]
f_{ch}	Fanning friction factor in channel	V_p	Velocity in plenum [m/s]
f_{app}	Apparent friction factor	W_w	Fin width [m]
H_{ch}	Channel height [m]	W_{ch}	Channel width [m]
h	Convective heat transfer coefficient [W/m².K]	W	Heat sink width [m]
h_x	Local heat transfer coefficient [W/m².K]	x^+	Dimensionless hydrodynamic axial distance
I	Current [A]	x^*	Dimensionless thermal axial distance
k_s	Thermal conductivity of copper block [W/m.K]		
K_c	Contraction loss coefficients	**Greek symbols**	
K_e	Expansion loss coefficients	$\propto$	Aspect ratio [W_{ch}/H_{ch}]
k_f	Thermal conductivity of fluid [W/m.K]	ξ	The excess loss coefficient of bend
K_{90}	The bend loss coefficient, (=1.2)	η_f	Fin efficiency
L	Heat sink Length [m]	ρ_f	Fluid density [kg/m³]
L_{ch}	Channel length [m]	μ_f	Dynamic viscosity of fluid [kg/m s]
n	Number of microchannel	ε	Channel surface roughness [μm]
Nu	Nusselt number		
ΔP_{ch}	Channel pressure drop [Pa]	**Subscripts**	
ΔP_t	Total pressure drop [Pa]	avg	Average
Pr	Prandtl number	f	Fluid (Water)
P_w	The wetted perimeter	in	Inlet
Q_{in}	Volumetric flow rate [m³/sec]	out	Outlet
q	Heat transfer rate [W]	max	Maximum
q_{loss}	Heat loss [W]	s	Solid
Re	Reynolds number	tci	Location of the thermocouple along the flow channel
R_{th}	Total thermal resistance [°C/W]	Γ	Interface between the fluid and solid

References:

[1] International Technology Roadmap for Semiconductors (ITRS), Semiconductor Industry Association (2010), http://www.ITRSnemi.org.

[2] I. Mudawar, Two-Phase Microchannel Heat Sinks: Theory, Applications, and Limitations, ASME J. Electron. Packaging, 133(4) (2011), p. 041002.

[3] B. Agostini, M. Fabbri, J.E. Park, L. Wojtan and J.R. Thome, State of the art of high heat flux cooling technologies, Heat Transfer Eng., 28 (2007) 258-281.

[4] J.R. Thome, State-of-the-Art Overview of Boiling and Two-Phase Flows in Microchannels, Heat Transfer Engineering, 27 (2006) 4-19.

[5] D.B. Tuckerman and R.F.W. Pease, High-performance heat sinking for VLSI, IEEE Electron Device Letters EDL 2 (5) (1981) 126–129.

[6] B.H. Salman, H.A. Mohammed, K.M. Munisamy,A. Sh. Kherbeet, Characteristics of heat transfer and fluid flow in microtube and microchannel using conventional fluids and nanofluids: A review, Renewable and Sustainable Energy Reviews 28 (2013) 848–880.

[7] R.J. Philips, Forced-convection, liquid-cooled microchannel heat sinks, Master Thesis, Massachusetts Institute of Technology, Cambridge, MA, 1987.

[8] X.F. Peng, G.P. Peterson, The effect of thermofluid and geometrical parameters on convection of liquids through rectangular microchannels, Int. J. Heat Mass Transfer 38 (4) (1995) 755–758.

[9] X.F. Peng, G.P. Peterson, Convective heat transfer and flow friction for water flow in microchannels structures, Int. J. Heat Mass Transfer 39 (12) (1996) 2599–2608.

[10] W. Qu, I. Mudawar, Analysis of three-dimensional heat transfer in micro-channel heat sinks, Int. J. Heat Mass Transfer 45 (2002) 3973–3985.

[11] K. Kawano, K. Minakami, H. Iwasaki, M. Ishizuka, Micro channel heat exchanger for cooling electrical equipment, Application of Heat Transfer in Equipment, Systems and Education, ASME HTD-361-3/PID-3 (1998) 173–180.

[12] H.Y. Wu, P. Cheng, An experimental study of convective heat transfer in silicon microchannels with different surface conditions, Int. J. Heat Mass Transfer 46 (2003) 2547–2556.

[13] J.P. McHale, S.V. Garimella, Heat transfer in trapezoidal microchannels of various aspect ratios, Int. J. Heat Mass Transfer 53 (1–3) (2010) 365–375.

[14] Y.T. Yang, S.C. Liao, Numerical optimization of trapezoidal microchannel heat sinks, International Journal of Mechanical, Aerospace, Industrial and Mechatronics Engineering 8 (8) (2014) 1374 - 1377.

[15] I. Tiselj, G. Hetsroni, B. Mavko, A. Mosyak, E. Pogrebnyak, Z. Segal, Effect of axial conduction on the heat transfer in micro-channels, Int. J. Heat Mass Transfer 47 (2004) 2551–2565.

[16] G.P. Celata, M. Cumo, V. Marconi, S.J. McPhail, G. Zummo, Microtube liquid single-phase heat transfer in laminar flow, Int. J. Heat Mass Transfer 49 (2006) 3538–3546.

[17] C. Nonino, S. Savino, S. Del Giudice, L. Mansutti, Conjugate forced convection and heat conduction in circular microchannels, Int. J. Heat Fluid Flow 30 (5) (2009) 823–830.

[18] S.X. Zhang, Y.L. He, G. Lauriat, W. Tao, Numerical studies of simultaneously developing laminar flow and heat transfer in microtubes with thick wall and constant outside wall temperature, Int. J. Heat Mass Transfer 53 (2010) 3977– 3989.

[19] J. Zhang, P.T. Lin, Y. Jaluria, Design and optimization of multiple microchannel heat transfer systems, Journal of Thermal Science and Engineering Applications 6 (1) (2014) 011004.

[20] Y. Sui, C.J. Teo, P.S. Lee, Y.T. Chew, C. Shu, Fluid flow and heat transfer in wavy microchannels, International Journal of Heat and Mass Transfer 53 (2010) 2760–2772.

[21] Y. Sui, P.S. Lee, C.J. Teo, An experimental study of flow friction and heat transfer in wavy microchannels with rectangular cross section, International Journal of Thermal Sciences 50 (2011) 2473-2482.

[22] R.H. Vafaie, M. Mahdipour, H. Mirzajani, H.B. Ghavifekr, Numerical Simulation of Mixing Process in Tortuous Microchannel, Sensors & Transducers, 151 (2013) 30-35.

[23] Z. Dai, D. F. Fletcher , B. S. Haynes, Impact of tortuous geometry on laminar flow heat transfer in microchannels, International Journal of Heat and Mass Transfer 83 (2015) 382–398.

[24] X. Hao, B. Peng, G. Xie, Y. Chen, Thermal analysis and experimental validation of laminar heat transfer and pressure drop in serpentine channel heat sinks for electronic cooling. Journal of Electronic Packaging, 136(3) 2014, 031009.

[25] H.A. Mohammed, P. Gunnasegaran, N.H. Shuaib, Numerical simulation of heat transfer enhancement in wavy microchannel heat sink, International Communication in Heat Mass Transfer 38 (2011) 63-68.

[26] H.A. Mohammed, P. Gunnasegaran, N.H. Shuaib, Influence of channel shape on the thermal and hydraulic performance of microchannel heat sink, International Communication in Heat and Mass Transfer 38 (2011) 474–480.

[27] Y. Chen, B. Penguins, X. Hao, G. Xie, Fast approach of Pareto-optimal solution recommendation to multi-objective optimal design of serpentine-channel heat sink, Applied thermal engineering 70 (2014) 263-273.

[28] R.H. Shih, P.J. Schilling, Parametric Modeling with SolidWorks 2015, 2015, New Orleans, Louisiana.

[29] S.G. Kandlikar, S. Garimella, D. Li, S. Colin, M.R. King, S.G. Kandlikar, chapter 3-Single-phase liquid flow in minichannels and microchannels, in: Heat Transfer and Fluid Flow in Minichannels and Microchannels, 2014, pp 103-174.

[30] R.K. Shah, A correlation for laminar hydrodynamic entry length solutions for circular and noncircular ducts, ASME Journal of Fluids Engineering 100 (1978) 177-179.

[31] I.E. Idelchik,, Handbook of Hydraulic Resistance, Hemisphere Publishing, 1986, New York, NY.

[32] W.M. Kays, A.L. London, Compact Heat Exchangers, 3rd edition, 1984, McGraw-Hill, New York, NY.

[33] S. Maharudrayya, S. Jayanti, A.P. Deshpande, Pressure losses in laminar flow through serpentine channels in fuel cell stacks. J Power Sources 138 (2004) 1–13.

[34] ASME. Test uncertainty. PTC 19.1-1998. American Society of Mechanical Engineers, New York, 1998.

[35] H.W. Coleman, W.G. Steele Experimentation, validation, and uncertainty analysis for engineers, 3rd edition, 2009, John Wiley and Son. Inc., Hoboken, New Jersey, USA.

[36] C.S. Sharma, M.K. Tiwari, B. Michel, D. Poulikakos, Thermofluidics and energetics of a manifold microchannel heat sink for electronics with recovered hot water as working fluid, International Journal of Heat and Mass Transfer 58 (2013) 135–151.

[37] B.C. Dhindsa, K. Pericleous, Investigation into the performance of turbulence models for fluid flow and heat transfer phenomena in electronic applications, IEEE Trans. Compon. Packag. Technol. 28 (4) (2005) 686-699.

[38] D.C. Wilcox, Turbulence modelling for CFD. Vol. 2. 1998: DCW industries La Canada, CA.

[39] W.M. Kays, "Turbulent Prandtl Number — Where Are We?", ASME J. Heat Transfer, vol. 116, pp. 284–295, 1994

[40] S.G. Kandlikar, S. Joshi, S. Tian, Effect of surface roughness on heat transfer and fluid flow characteristics at low Reynolds numbers in small diameter tubes, Heat Transfer Engineering, 24 (3) (2003) 4 – 16.

[41] R.K. Shah, A.L. London, Laminar flow forced convection in ducts, 1978, Academic press, New York.

[42] P.S. Lee, S.V. Garimella, D. Liu, Investigation of heat transfer in rectangular microchannels, International Journal of Heat and Mass Transfer 48 (2005) 1688–1704.

[43] P.S. Lee, S.V. Garimella, Thermally developing flow and heat transfer in rectangular microchannels of different aspect ratios, International Journal of Heat and Mass Transfer 49 (2006) 3060–3067.

[44] P.W. Dittus, L.M.K. Boelter, Heat transfer in automobile radiators of the tubular type, Univ. Calif. Publ. Eng. 2(13) (1930) 443–461; reprinted in Int. Commun. Heat Mass Transfer, 12 (1985) 3–22.

[45] Z. Dai, D.F. Fletcher, B.S. Haynes, Impact of tortuous geometry on laminar flow heat transfer in microchannels, International Journal of Heat and Mass Transfer 83 (2015) 382–398.

[46] M.E. Steinke, S.G. Kandlikar, Single-phase liquid heat transfer in plain and enhanced microchannels, in: Proceedings of fourth international conference on nanochannels, Microchannels and minichannels, Limerick, Ireland, 2006.

[47] O. Manca, S. Nardini, D. Ricci, A numerical study of nanofluid forced convection in ribbed channels, Applied Thermal Engineering, 37 (2012) 280-292.

[48] N.R. Rosaguti, D.F. Fletcher, B.S. Haynes, Laminar flow and heat transfer in a periodic serpentine channel with semi-circular cross-section, International Journal of Heat and Mass Transfer 49 (2006) 2912–2923.

<div align="center">

Supplementary Information

An experimental and numerical investigation of the use of liquid flow in serpentine microchannels for microelectronics cooling

</div>

Ahmed F. AL-Neama [a,b,1] , Nikil Kapur [a], Jonathan Summers [a], Harvey M. Thompson [a]

[a] Institute of Thermofluids, School of Mechanical Engineering, University of Leeds, LS2 9JT, United Kingdom.

[b] Department of Mechanical Engineering, Faculty of Engineering, University of Mosul, Iraq.

Section 1:

Table 1
Friction factor correlation for single-phase flow in MCHS.

Author [Ref.]	Published correlation equation	Eq.	Geometry	Flow regime	Range of validity
Shah and London [41]	$f_{lam,fd} = \frac{24}{Re}(1 - 1.3553 \propto +1.9467 \propto^2 - 1.7012 \propto^3 + 0.9564 \propto^4 - 0.2537 \propto^5)$	S.1	Rectangular	Fully developed laminar	Re < 2300
Shah [30] Lee and Qu [S1]	$f_{app\_Laminar} = \frac{3.44}{Re\sqrt{x^+}} + \frac{(f_{lam,fd} \cdot Re) + \frac{K(\infty)}{4x^+} - \frac{3.44}{\sqrt{x^+}}}{Re\left(1 + \frac{C}{x^{+2}}\right)}$ $K(\infty) = 0.674 + 1.2501 \propto + 0.3417 \propto^2 - 0.8358 \propto^3$ $C = (0.1811 + 4.3488 \propto +1.6027 \propto^2) \times 10^{-4}$	S.2	circular and non-circular channels	Developing flow laminar	Re < 2300
Phillips [7]	$f_{turb\_Phillips} = \left(0.0929 + \frac{1.01612}{\left(\frac{L_{ch}}{D_h}\right)}\right) Re_{eq}^{\left(-0.268 - \frac{0.3193}{\left(\frac{L_{ch}}{D_h}\right)}\right)}$ $Re_{eq} = \frac{\rho_f \cdot V_{ch} \cdot D_{h_{eq}}}{\mu_f}$, $D_{h_{eq}} = D_h\left(\frac{2}{3} + \frac{11\propto(2-\propto)}{24}\right)$	S.3	Rectangular	Developing flow turbulent	$3000 < Re < 10^5$

Table 2
Heat transfer correlation for single-phase flow in MCHS.

Author [Ref.]	Published correlation equation	Eq.	Geometry	Flow regime	Range of validity
Lee and Garimella [43]	$Nu_{4,x} = \frac{1}{C_1(x^*)^{C_2+C_3}} + C_4 \quad for \quad x^* < x^*_{th}$ Where x^*_{th} denotes the length of the thermally developing region as: $x^*_{th} = \frac{-1.275\times10^{-6}}{\propto^6} + \frac{4.709\times10^{-5}}{\propto^5} - \frac{6.902\times10^{-4}}{\propto^4} + \frac{5.014\times10^{-3}}{\propto^3} - \frac{1.769\times10^{-2}}{\propto^2} + \frac{1.845\times10^{-2}}{\propto} + 0.05691$ $C_1 = \frac{-2.757\times10^{-3}}{\propto^3} + \frac{3.274\times10^{-2}}{\propto^2} - \frac{7.464\times10^{-5}}{\propto} + 4.476$ $C_2 = 0.6391$ $C_3 = \frac{1.604\times10^{-4}}{\propto^2} - \frac{2.622\times10^{-3}}{\propto} + 2.568 \times 10^{-2}$ $C_4 = 7.301 - \frac{13.11}{\propto} + \frac{15.19}{\propto^2} - \frac{6.094}{\propto^3}$	S.4	Rectangular	Thermally developing laminar flow	Re < 2300
Shah and London [41]	$Nu_{3,fd\_lam} = 8.235 (1 - 1.883 \propto + 3.767 \propto^2 - 5.814 \propto^3 + 5.361 \propto^4 - 2 \propto^5)$	S.5	Rectangular	Fully developed laminar	Re < 2300
	$Nu_{4,fd\_lam} = 8.235 (1 - 2.0421 \propto + 3.0853 \propto^2 - 2.4765 \propto^3 + 1.0578 \propto^4 - 0.1861 \propto^5)$	S.6	Rectangular	Fully developed laminar	Re < 2300
Dittus-Boelter [44]	$Nu_{Dittus-Boelter,fd\_turb} = 0.023.Re^{0.8}.Pr^{0.4}$	S.7	Circular	Fully developed turbulent	$3000 < Re < 10^5$

---

[*] Corresponding author. E-mail address: ahmedfalneama@gmail.com (Ahmed F. AL-Neama).

Section 2:

Table 3

Uncertainty of various critical MCHS parameters.

Variable	Total relative uncertainties
Channel widt (W_{ch})	±0.60%, ±0.4%
Channel height (H_{ch})	±0.30%, ±0.2%
Channel length (L_{ch})	±0.03%, ±0.002%
Fin width (W_w)	±0.6%
Hydraulic diameter (D_h)	±0.41%, ±0.27%
Volumetric flow rate (Q_{in})	±2.5% − ±0.083%
Temperature (T)	±0.3%
Nusselt number (Nu)	±3.7% − ±9%
Pressure drop (ΔP)	±2.6% − ±15.2%
Friction factor (f)	±3.4% − ±16.3%
Thermal resistance (R_{th})	±2.8% − ±7.3%

The final uncertainty equations associated with f_{ch}, Nu and R_{th} for SRM Heat Sink are given as:

$$\frac{U_{f_{ch}}}{f_{ch}} = \sqrt{\left(\frac{U_{\Delta P_{ch}}}{\Delta P_{ch}}\right)^2 + \left(\frac{U_\rho}{\rho}\right)^2 + \left(\frac{U_{L_{ch}}}{L_{ch}}\right)^2 + 4\left(\frac{U_Q}{Q}\right)^2 + 9\left(\frac{U_{W_{ch}}}{W_{ch}}\right)^2 + \left(\frac{U_{W_{ch}}}{H_{ch}+W_{ch}}\right)^2 + 9\left(\frac{U_{H_{ch}}}{H_{ch}}\right)^2 + \left(\frac{U_{H_{ch}}}{H_{ch}+W_{ch}}\right)^2} \quad \text{(S.8)}$$

$$\frac{U_{Nu}}{Nu} = \pm\sqrt{\left(\frac{U_V}{V}\right)^2 + \left(\frac{U_I}{I}\right)^2 + \left(\left(\frac{T_w}{T_w-T_f}\right)\frac{U_{T_w}}{T_w}\right)^2 + \left(\left(\frac{T_f}{T_w-T_f}\right)\frac{U_{T_f}}{T_f}\right)^2 + \left(\frac{U_{A_{eff}}}{A_{eff}}\right)^2 + \left(\frac{U_{k_f}}{k_f}\right)^2 + \left(\frac{U_{D_h}}{D_h}\right)^2} \quad \text{(S.9)}$$

$$\frac{U_{R_{th}}}{R_{th}} = \pm\sqrt{\left(\frac{U_V}{V}\right)^2 + \left(\frac{U_I}{I}\right)^2 + \left(\left(\frac{T_w}{T_w-T_f}\right)\frac{U_{T_w}}{T_w}\right)^2 + \left(\left(\frac{T_f}{T_w-T_f}\right)\frac{U_{T_f}}{T_f}\right)^2} \quad \text{(S.10)}$$

Properties of water such as fluid density, dynamic viscosity, specific heat, Prandtl number (Pr) and thermal conductivity (k) were determined according to the tabulated values in Incropera and DeWitt [S2], leading to uncertainties in the fluid properties of around 0.5%. By using the estimated errors of the parameters listed in Table 3, the experimental uncertainty for Re, f_{ch}, R_{th} and Nu can be calculated.

Section 3:

To predicate the excess bend loss coefficient (ξ) in SPSM heat sink design, Maharudrayya et al. [33] carried out a CFD simulation of laminar single-phase flow through 180° bends and serpentine rectangular channels, and three-regime correlation was proposed to determine the ξ as a function of the Reynolds number ($0 < Re = \frac{\rho_f \cdot v_{ch} \cdot D_h}{\mu_f} < 2200$), aspect ratio ($1 < \alpha = \frac{H_{ch}}{W_{ch}} < 6$), curvature ratio ($0 < C = \frac{R_c}{D_h} < 6$) and fin width as follows:

For < 100 :

$$\xi = 0 \quad \text{(S.11a)}$$

For $100 < Re < 1000$:

$$\xi = 0.46(Re)^{1/3}(1 - 0.18C + 0.016C^2) \times (1 - 0.2\alpha + 0.0022\alpha^2) \times \left(1 + 0.26\left(\frac{W_w}{D_h}\right)^{2/3} - 0.0018\left(\frac{W_w}{D_h}\right)^2\right) \quad \text{(S.11b)}$$

For $1000 < Re < 2200$:

$$\xi = 3.8(1 - 0.22C + 0.022C^2) \times (1 - 0.1\alpha + 0.0063\alpha^2) \times \left(1 + 0.12\left(\frac{W_w}{D_h}\right)^{2/3} - 0.0003\left(\frac{W_w}{D_h}\right)^2\right) \quad \text{(S.11c)}$$

where R_c represents the mean radius of the bend.

The pressure distribution in every straight microchannel in SPSM heat sink is represented by the maximum and minimum pressure, which are given by [S3]:

$$P_{min} = \Delta P_{t\_SPSM} - (i-1)\frac{1}{2} \cdot \rho_f \cdot V_{ch}^2 \left(4 f_{app} \cdot \frac{L_{ch}}{D_h} + \xi\right) \tag{S.12}$$

$$P_{max} = \Delta P_{t\_SPSM} - \frac{1}{2} \cdot \rho_f \cdot V_{ch}^2 \left(4i f_{app} \cdot \frac{L_{ch}}{D_h} + (i-1)\xi\right) \tag{S.13}$$

Section 4:

Fig. S1 shows the mesh in TPSM heat sink design and resolution was increased near the bends.

Table 4
Validation of grid independence.

	Straight rectangular MCHS (SRM)								Single path multi-serpentine rectangular MCHS (SPSM)							
	1 (0.979×10^6)	E%	2 (1.897×10^6)	E%	3 (2.637×10^6)	E%	4 (3.356×10^6)		1 (0.937×10^6)	E%	2 (1.992×10^6)	E%	3 (2.788×10^6)	E%	4 (4.834×10^6)
$T_{junction}$ (℃)	57.4	5.7	56.0	3.1	55.0	1.3	54.3		47.4	7.5	46.0	4.3	44.9	1.8	44.1
Nu_{avg}	9.7	9.0	9.3	4.5	9.1	2.2	8.9		14.3	8.3	13.8	4.6	13.5	2.3	13.2

|	Double path multi-serpentine rectangular MCHS (DPSM)								Triple path multi-serpentine rectangular MCHS (TPSM)							
	1 (0.852×10^6)	E%	2 (1.836×10^6)	E%	3 (2.526×10^6)	E%	4 (3.703×10^6)		1 (0.844×10^6)	E%	2 (1.776×10^6)	E%	3 (2.486×10^6)	E%	4 (3.649×10^6)
$T_{junction}$ (℃)	51.3	6.2	49.4	2.3	48.9	1.2	48.3		54.0	8.0	52.6	5.2	51.0	2.0	50
Nu_{avg}	12.8	7.5	12.4	4.2	12.1	1.7	11.9		11.4	8.6	11.0	4.8	10.7	1.9	10.5
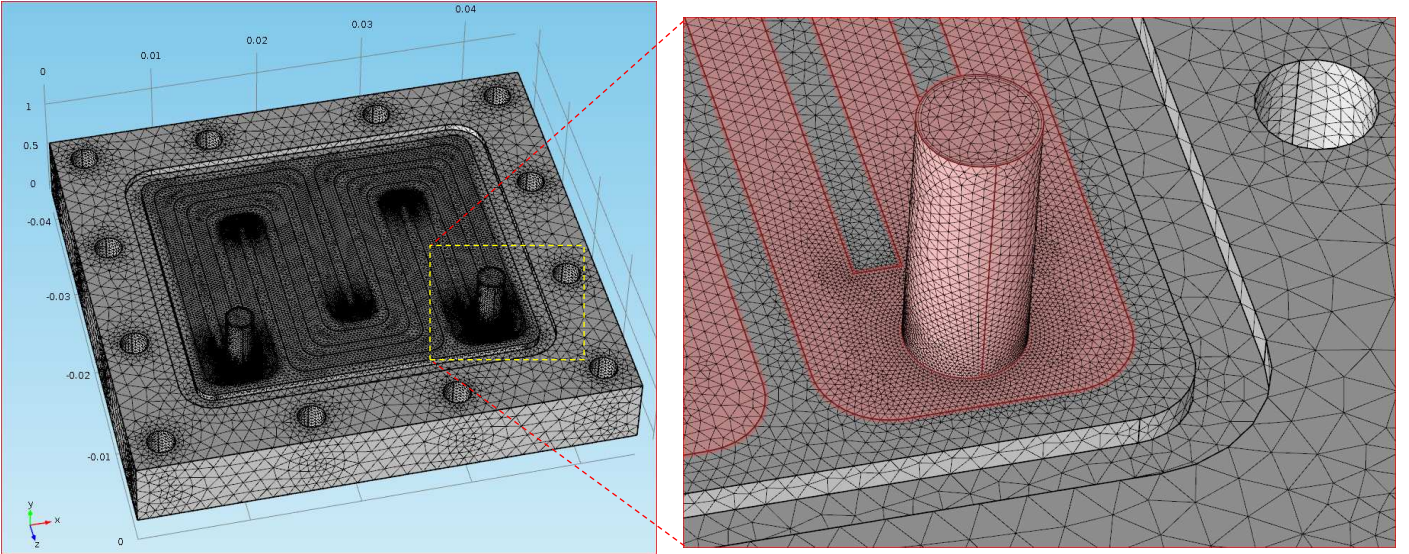
Fig. S1: Numerical mesh using case 3 for a TPSM design.

References

[S1] S.W. Lee, W. Qu, Thermal design methodology for low flow rate single-phase and two-phase micro-channel heat sinks, IEEE Transactions on components and packaging technologies, 30(4) (2007) 830-841.

[S2] T.L Bergman, A.S. Lavine, F.P. Incropera and D.P. DeWitt, Fundamentals of Heat and Mass Transfer, 2011, New York: John Wiley and Sons.

[S3] X.H. Hao, X.K. Li, B. Peng, M. Zhang, Y. Zhu, Thermal Resistance Network Model for Heat Sink with Serpentine Channel, Int. J. Numer. Modell.: Electron. Networks, Devices Fields, 27(2) (2013), 298–308.